CHAPTER 3

Template electrodeposition of nickel and electron transfer studies using a lyotropic liquid crystalline phase, a microemulsion phase and micelles as electrolytic media

This chapter deals with a template electrodeposition of nickel and its characterization using a variety of surface, microscopic and electrochemical techniques and electron transfer studies of redox probe molecules such as $[Fe(CN)_6]^{3-|4-}$ and $[Ru(NH_3)_6]^{2+|3+}$ using some self-aggregated systems of surfactant as electrolytic media. We have used a new hexagonal lyotropic liquid crystalline phase and a microemulsion phase as templates for the electrodeposition of nickel and in addition to these two phases we have also used micelles for electron transfer studies. In this kind of template electrodeposition, we find that the mass transfer plays a vital role in determining the surface properties, the nature and structure of the deposited materials. In this connection, we also find a similar enhancement in the mass transfer leading to a fine grain growth of nickel when the electrodeposition was carried out in presence of an external magnetic field.

This chapter has been divided into four parts. The first part deals with the study of electrodeposition of nickel using a new hexagonal liquid crystalline phase as a template. The second part provides a detailed study on the effect of applied magnetic field on the electrodeposition of nickel. The third part consists of template electrodeposition of nickel and its characterization using a microemulsion phase as a template. The fourth and final part deals with the

electron transfer studies of redox probe molecules using some self-aggregated systems of surfactants as electrolytic media.

I. A HEXAGONAL LIQUID CRYSTALLINE PHASE AS A TEMPLATE

3.1. Introduction

The process of depositing a metal or metal oxide through a template to produce pattern on the surface by the process of electrolysis is known as "template electrodeposition". Mostly this kind of deposition is employed to prepare the nanomaterials of desired size, shape and properties. Depending on the structure of template used for the deposition of materials, we can produce surfaces having different desired structures. The templates normally used for the electrodeposition can be broadly classified into two categories namely the ***hard*** and ***soft*** templates. The hard templates involve the usage of anodized alumina, polycarbonate, porous silica, mica, carbon nanotubes and zeolites etc. On the other hand, the soft template consists mainly of surfactant aggregate systems such as micelles, reverse micelles, microemulsion and mesophases like lyotropic hexagonal, reverse hexagonal and lamellar phases. Usually, the soft templates are preferred over the hard templates due to the easier removal of the same after the deposition. The microemulsion forms spherical aqueous microdomains of nanometer dimensions through which the electrodeposition occurs. In the other cases, deposition of metals or metal oxides occurs through the nanoporous templates producing different nanostructured materials such as nanowires, nanodisks, nanoparticles, nanohorns, nanorods etc. depending upon the size and shape of the template used.

Template electrodeposition of different metals in various surfactant aggregate systems like hexagonal liquid crystalline phases [1,2], reverse hexagonal liquid crystalline phases [3] and emulsion phases [4,5] is being

studied extensively in recent times due to its importance in nanotechnology, electrocatalysis, supercapacitors and fuel cells. There have also been several reports on template chemical synthesis using lyotropic liquid crystalline phases [6,7], microemulsion phases [8,9] and colloids [10]. Apart from the surfactant systems, anodized aluminium oxide [11] and polystyrene spheres [12] are also being used as hard templates for electrochemical deposition of various metals and metal oxides.

Surfactant mesophases come under the category of soft template systems and electrodeposition through them is a very useful and versatile method for the synthesis of nanostructured materials. This approach overcomes the problems such as fabrication and dissolution of the templates normally associated with the hard template techniques. Besides, the lyotropic liquid crystalline phases possess a long-ranged spatially periodic architecture with their lattice parameters in the range of a few nanometers. This makes them ideal candidate systems for the synthesis of nanomaterials.

Attard et al. [1] have reported the electrochemical deposition of highly ordered nanoporous platinum films having a high specific surface area, electrical connectivity, fast electrolyte diffusion and good mechanical and electrochemical stability using a lyotropic liquid crystalline phase as a template. This method has been further used as a general synthetic technique for producing metal films containing a lattice of periodic channels with nanometer dimensions. The basic principle of this method involves electrodepositing the required metal or material through the channels provided by the template present in the electrolyte to access the conductive substrate, where the deposition occurs. For this purpose, the lyotropic liquid crystal template needs to be in intimate contact with the substrate and acts as a mask for deposition only on the selected regions of the surface.

The preparation and study of high true surface area nickel and its alloys are of interest as they are used as hydrogen evolving cathodes in electrocatalysis and in many industrial electrochemical processes and also as batteries in electrochemical energy storage devices. For example, Simpraga et al. obtained a very high roughness factor value of the order of 2800 for Ni-Fe composite electrodes prepared by a simple electrochemical co-deposition process [13]. Rausch and Wendt characterized the high surface area sintered Ni and Raney Ni for their electrocatalytic properties using Tafel plot analysis and electrochemical impedance spectroscopic studies [14]. Brown and Sotiropoulos reported the preparation of a highly porous nickel deposit having a large surface area using a high internal phase emulsion (HIPE) as a template [15]. This is basically a water–in-oil emulsion where the water content exceeds 75% v/v. They obtained a highly porous deposit having irregular structure that shows relatively a low overpotential for hydrogen evolution reaction (her) on its surface. It was shown that the materials prepared by HIPE template deposition technique are more effective than sintered nickel in its electrocatalytic activity.

There have been a several reports in the literature on nickel oxide (NiO) being used as a supercapacitor electrode material [16-19]. These reports are mainly based on the electrochemical precipitation of $Ni(OH)_2$ followed by heating in air at various temperatures to obtain nickel oxide. The specific capacitance values reported vary from 50 F/g to 277 F/g of nickel oxide [16], depending upon the procedure employed for the preparation of nickel oxide material. These very high measured capacitance values are attributed to the increase in true surface area [17] as well as to the non-stoichiometric nature of nickel oxide material [18]. Recently, Nelson and Owen have reported a high performance nanostructured Ni(OOH), which is obtained by a liquid crystal

templating technique [19]. This mesoporous material can be effectively used as a positive electrode in the hybrid supercapacitors/battery systems.

In this section, the studies performed on template-electrodeposited nickel material and its characterization methods have been explained in a detailed manner. We have carried out a very simple process to prepare a high surface area mesoporous nickel deposit, using a new hexagonal liquid crystalline phase as a template. This room temperature deposited nickel material has been characterized using electrochemical techniques such as cyclic voltammetry (CV), electrochemical impedance spectroscopy (EIS) and Tafel plot analysis. Besides these techniques, we have also performed scanning electron microscopy (SEM), scanning tunneling microscopy (STM) and X-Ray diffraction (XRD) studies for surface characterization of this material.

3.2. Experimental section

3.2.1. Chemicals

Triton X-100 (Spectrochem), poly(acrylic acid) (PAA) (Aldrich), sodium hydroxide pellets (EMerck), nickel (II) chloride (EMerck), nickel sulphamate (Grauer and Wheel) and boric acid (Sarabhai chemicals) were used in this study. All the chemical reagents used were AnalaR (AR) grade. Millipore water having a resistivity of 18 MΩ cm was used in all the experiments that have been performed at room temperature.

3.2.2. Preparation and characterization of a hexagonal liquid crystalline phase

A hexagonal liquid crystalline phase was prepared from a ternary mixture of Triton X-100, poly(acrylic acid) (PAA) and water [20]. The mixture exists in the hexagonal liquid crystalline phase at the room temperature of 25^0C

and increasing the concentrations of PAA shifts the phase transition to isotropic phase at a temperature above 29^0C. We have carried out our studies at two different weight compositions viz., (1) Triton X-100 42% + Water 58% and (2) Triton X-100 42% + PAA 5% + water 53%. The mixture was stirred in a magnetic stirrer at a temperature of 33^0C – 35^0C for about 1 hour and was allowed to cool down to room temperature. When viewed under a polarized light microscope, the mixture exhibits the characteristic birefringence of a hexagonal liquid crystalline phase, which is stable up to 29^0C. In the textural studies of this liquid crystalline phase, we have observed the focal conic and broken mosaic textures corresponding to the hexagonal phase of the ternary system. And there is no texture observed when it undergoes a phase transition to isotropic phase at a temperature above 29^0C. Figure 1 shows the texture obtained for this phase when viewed under a polarized light microscope. All the electrodeposition experiments carried out using this hexagonal phase as a template have been performed at the room temperature of 25^0C.

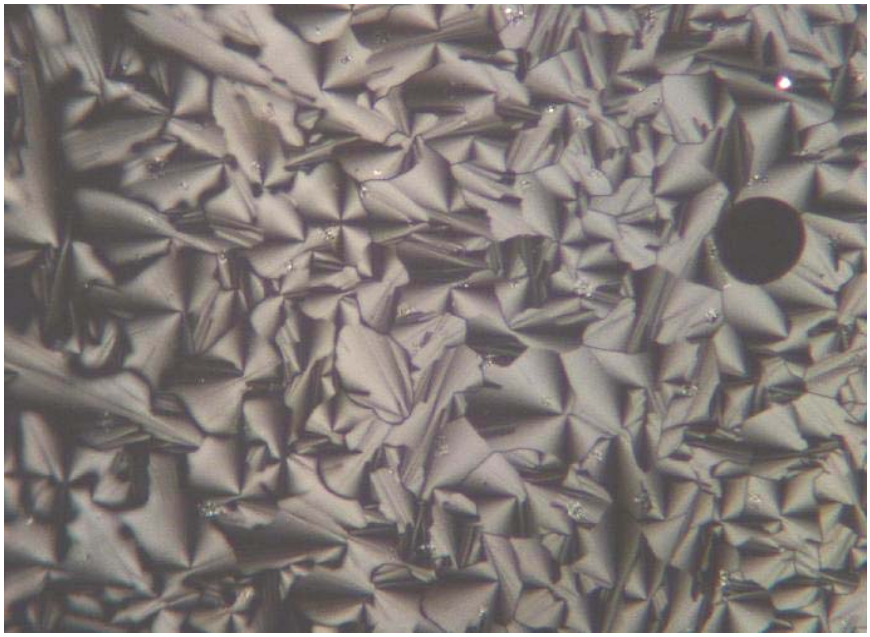

Figure 1: Polarizing light microscopic texture corresponding to hexagonal liquid crystalline phase used in this study.

3.2.3. Nickel electrodeposition through the hexagonal liquid crystalline phase

For electrodeposition, we have replaced the aqueous phase of the above-described hexagonal liquid crystalline system using the standard nickel sulphamate bath [21] having the composition: 300 g/l nickel sulphamate, 6 g/l nickel chloride and 30 g/l boric acid. The ternary system of Triton X-100, water and PAA containing the nickel salt solution in place of aqueous phase showed no optical birefringence under the polarizing light microscope at room temperature implying a change in the phase characteristics of the electroplating bath. However, this aspect has not been investigated further as it does not pertain to the present studies.

The typical size of a nickel strip used as substrate for electroplating is 1mm x 5mm x 5mm. These nickel substrates were cut from a 1mm thick Ni foil, which was prepared using the process of electroforming in nickel sulphamate bath of the same composition that has been used for the template electrodeposition of nickel. Before each experiment, the nickel substrate was polished successively in 1000, 1500 grade emery papers followed by polishing in 1μm, 0.3μm and finally in 0.05μm size alumina powder. Before electroplating, the nickel substrates were activated by immersion into a 1:1 HCl in water for a few seconds. A sulphurised nickel bar was used as an anode and the inter electrode distance was maintained at around 2 to 5 mm. The electroplating was carried out at different current densities of 2, 5, 7.5, and 10 mA/cm^2 at 25^0C for about 1-2 hours. The electrodeposited specimen were washed thoroughly with distilled water and then rinsed with millipore water and then immediately used for the analysis and its characterization. We have also studied the effect of deposition time by plating for 10, 30, 60, 90 and 120

minutes. Figure 2 shows the typical experimental setup used for this kind of electrodeposition.

The potential during the electrodeposition was monitored using chronopotentiometry. To ensure a perfectly smooth substrate for STM studies, we have electrodeposited nickel on a surface of gold that has been obtained by evaporation of gold on a mica sheet. In this case the nickel electroplating was carried out at a current density of 5 mA/cm^2 for about 10 minutes.

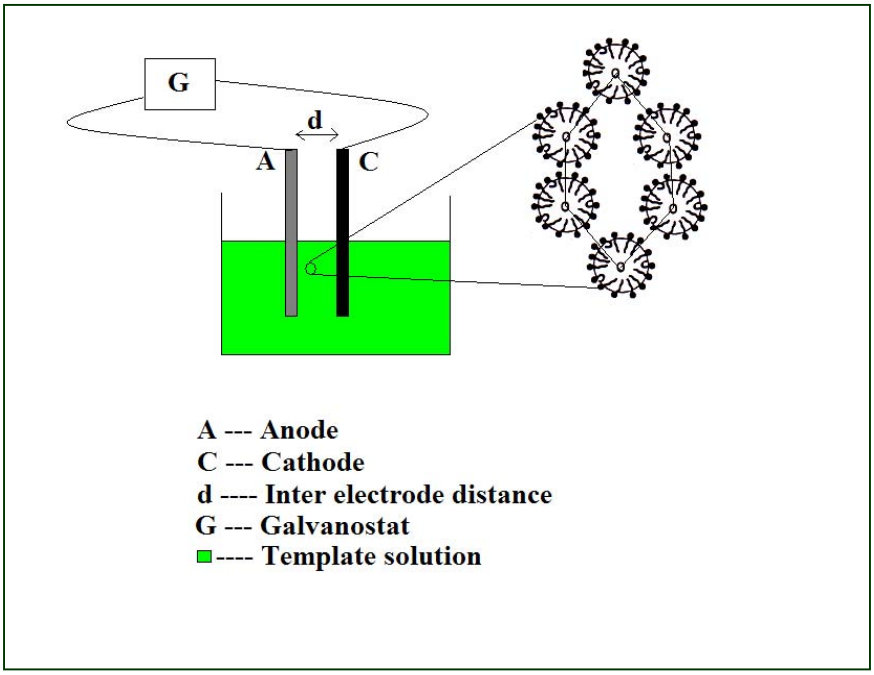

Figure 2: Schematic representation of the experimental setup used for template electrodeposition.

3.2.4. Characterization of nickel coated electrodes

(a). Using surface analytical techniques

SEM characterization of the template deposited materials has been done using JEOL JSM-840 A model instrument and the measurement parameters have been shown in the respective diagrams. Scanning tunneling microscopic studies have been carried out using a home-built instrument [22]

with an electrochemically etched tungsten tip as a probe. The images were collected under the constant current mode at a tunneling current of 1 nA and a substrate bias voltage of +100 mV. Roughness analysis of the STM data was performed using SPIP software (Image Metrology, Denmark). The STM was calibrated using a highly oriented pyrolytic graphite (HOPG) sample before carrying out the measurements.

X-ray diffraction measurements were carried out using a SHIMADZU X-ray diffractometer that uses a Cu-Kα radiation with a wavelength of 1.540 Å for the study. The 2θ value is varied from 20–80 degrees. The size of the particle is calculated from the full width at half maximum (FWHM) of the respective peak using Debye-Scherrer equation [23,24], which is given by,

$$\chi_s = (0.9 * \lambda) / (FWHM * \cos \theta) \qquad (1)$$

where χ_s is the crystallite size, λ the wavelength of X-ray used for the measurements and θ the diffraction angle.

(b). Using electrochemical techniques

Electrochemical characterization of the deposit was carried out in an all glass three-electrode electrochemical cell. A platinum foil of large surface area was used as a counter electrode and a saturated calomel electrode (SCE) as a reference electrode but kept in a separate compartment. Cyclic voltammetry was performed in the potential range of –1.3V to –0.2V vs. SCE in 0.5M NaOH aqueous solution at a potential scan rate of 50mV/s. Before the beginning of the experiments, the electrode was maintained at a potential of –1.6V vs. SCE for 600s in 0.5M NaOH solution. This process reduces the surface oxides present in the deposited material and cathodically cleans the surface by the evolution of hydrogen gas. This is followed by keeping the electrode at a potential of –1.02V

vs. SCE in order to oxidize any metal hydrides that are present on the surface. The potential is then scanned from –1.3V to –0.2V vs. SCE to obtain the nickel oxidation and reduction characteristics from which the electroactive surface area has been determined [15].

The chronoamperometric experiments for hydrogen evolution reaction were conducted by the application of a series of potential steps of 10–20 mV amplitude for a duration of 20s between –1.1V to –1.3V vs. SCE in a cell containing a separate compartment for the reference electrode. The potential data were corrected for ohmic drop due to the solution resistance R_u that has been determined using the current interruption technique.

The interfacial capacitance values of the template-deposited materials were determined using electrochemical impedance spectroscopic studies. These measurements were conducted in the hydrogen evolution region at different potentials at intervals of 50 mV between –1.2V and –1.4V vs. SCE. The EIS studies have been used earlier to understand the mechanism of hydrogen evolution reaction on the metal surfaces [14, 25-29]. The double layer capacitance value at this region is a direct measure of the true surface area accessible to the electrolyte for the hydrogen evolution reaction [14]. Besides, the EIS measurements provide useful information about the surface morphology including the pore structure [26, 27, 30-32].

The utility of these materials for supercapacitor applications have been investigated by potential scanning at the nickel oxide region [16-19]. First the potential was cycled between –0.1V and +0.5V vs. SCE for 25 cycles at 50 mV/s where the nickel oxide (NiO) formation and its stripping take place. The capacitance was then determined by scanning the as plated nickel electrode in the potential range from –0.1V to +0.25V vs. SCE at a scan rate of 50 mV/s for 25 cycles and measuring the integrated charge.

The cyclic voltammetric studies were performed using an EG&G potentiostat (model 263A) interfaced to a personal computer (PC) through a GPIB card (National Instruments). For electrochemical impedance spectroscopic studies the potentiostat is used along with an EG&G 5210 lock-in-amplifier controlled by a PC using the Power Sine software. The impedance measurements were carried out between 0.1 Hz and 100 kHz in all the cases. The ZSimpWin software program (EG&G) was used for the analysis of the impedance data and to determine various parameters using the equivalent circuit fitting procedure.

3.3. Results and discussion

3.3.1. Characterization of porous nickel deposit using SEM and STM

Figure 3 shows the SEM images of nickel surfaces obtained using template electrodeposition. Figure 3(a) shows the SEM image of the nickel surface electrodeposited at 5 mA/cm^2 current density for about 60 minutes using a new hexagonal liquid crystalline phase as a template. A well adherent deposit of high porosity and irregular structure has been obtained. These pores have an average diameter of typically 1-2μm and appear to extend to the full thickness of the coating. The clusters of granular nickel particles can be seen from the figure and it is found to be distributed more or less evenly in between the pores.

Figure 3(b) shows a higher magnification image of the nickel deposit showing the presence of Ni nanoparticles in between the pores and also inside of the pore walls. Typical size of these particles varies from 200 nm to 500 nm. A closer examination of these images suggests that these particles are actually made up of still smaller nanoparticles that agglomerate with each other to form

the clusters. This has been further examined by the scanning tunneling microscopy and the corresponding images are shown in figure 4.

It is well known in the liquid crystal literature that the binary system of Triton X-100 and water shows the hexagonal liquid crystalline phase [2, 34]. We have carried out the nickel electrodeposition in this phase also. Figure 3(c) shows the SEM picture of the nickel surface electrodeposited at 5 mA/cm^2 current density for about 60 minutes using the nickel-electroplating bath prepared in this liquid crystalline phase. In contrast to the ternary phase system described above, there is no formation of porous structure here though nickel nanocrystallites of sizes varying from 200 nm to 500 nm are clearly seen in the image. These aggregates of smaller particles constitute much bigger clusters of micrometer dimensions. The distribution of these particles is also quite uniform and dense throughout the surface. From this, it is therefore clear that the pore formation is unique only to the electrolyte formed in the ternary phase containing PAA.

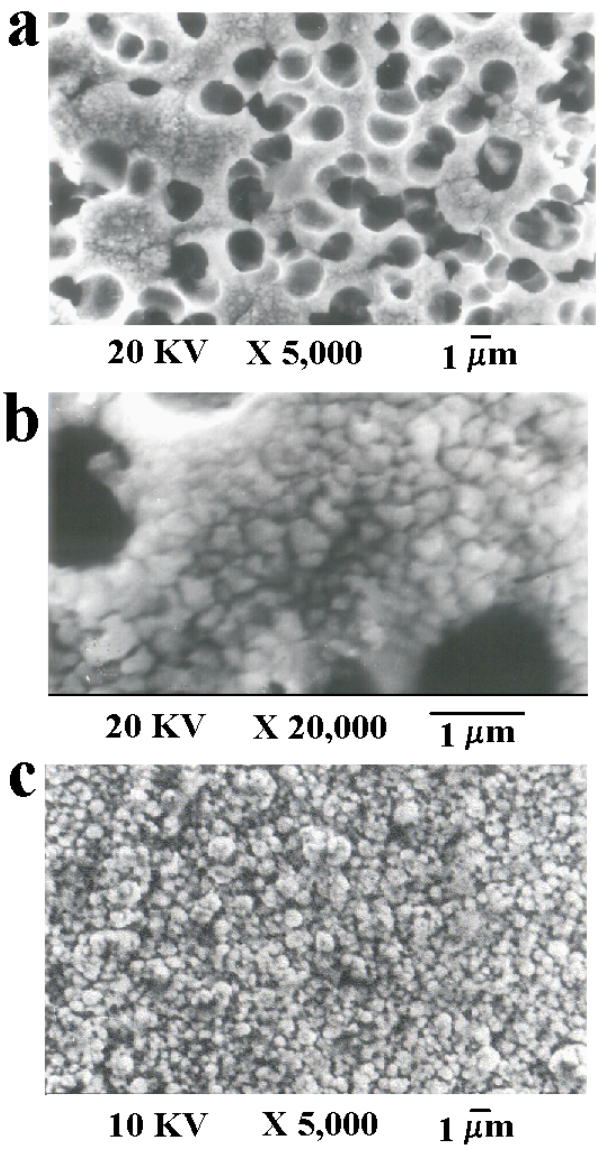

Figure 3: SEM micrographs of nickel electrodeposits prepared at 5 mA/cm^2 current density using: (a) Water -Triton X -100 - PAA composition as a template. (b) Same as (a) but with higher magnification at a different region showing the pores and clusters of nanoparticles formation. (c) Water -Triton X -100 (without PAA) as a template. The other parameters are shown in the respective diagrams.

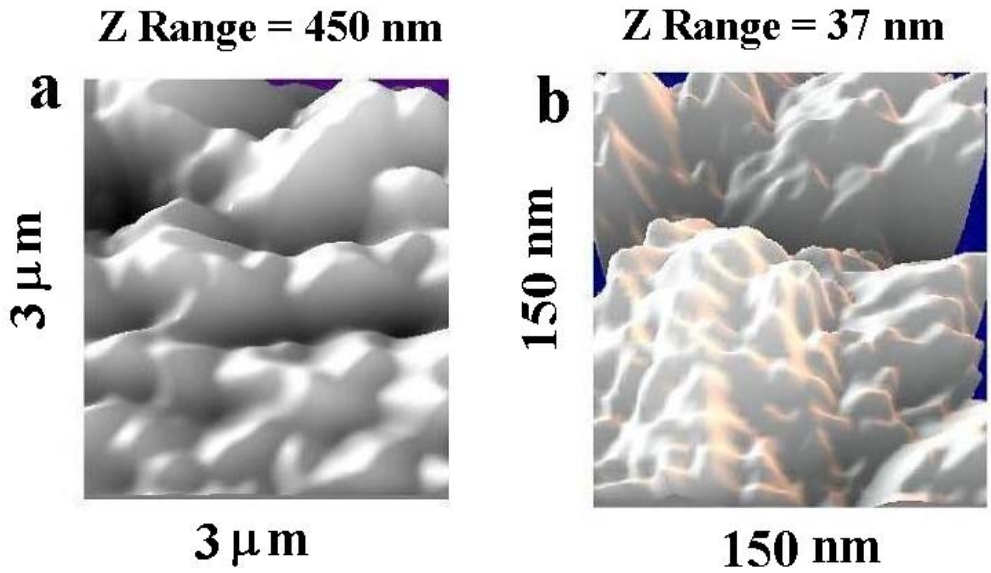

Figure 4: Constant current STM images: Tunneling current: 0.5 nA, Bias voltage: Sample + 100mV, (a) Scan range: 150nm x 150nm (b) 3µm x 3µm for an electroplated nickel on evaporated gold on mica using a new hexagonal liquid crystalline phase of Water - Triton X -100 - PAA composition as a template.

Figure 4 shows the STM images of the template deposited nickel surface at two different scan ranges. The 3µm x 3µm constant current STM image of the surface of porous nickel deposit is shown in figure 4(a). The average sizes of these crystals are about 300 nm to 500 nm at this range. The image of the nickel surface at a lower scan range of 150 nm x 150 nm, as shown in figure 4(b) shows the individual domains separated by deep grain boundary regions comprising of several nanocrystalline features of about 30 nm – 40 nm in size clustered together. A roughness analysis of the 3µm x 3µm image (Fig.

4(a)) shows an average roughness value of 177 nm and root mean square (RMS) roughness R_q of 49.5 nm. R_q is the root mean square of all the profile values of the roughness and it expresses the standard deviation of the surface height measurements and so provides information about the distribution of data. The surface area ratio parameter (S_{dr}), which expresses the ratio between the surface area (taking the Z height into account) and the area of the flat XY plane is measured to be 20.5, which is the roughness factor of the surface as measured by STM. Similar analysis of the surface of 150nm x 150nm image also shows relatively a higher roughness factor of 140. The difference in these two regimes is due to the difference in the length scales and resolution attainable in these two ranges [33]. In the higher resolution image of 150nm x 150nm scan range (Fig. 4(b)), the contribution to the overall surface area arises from the nanoscale roughness on the surface.

The origin of pore formation on the nickel electrodeposit prepared using the ternary system of water – Triton X-100 – PAA is not clear at this moment and beyond the scope of the present work. It is speculated that the porous structure is essentially due to the screening of the electrode to the flow of Ni ions by giant sized aggregates present in the ternary system, which shows a hexagonal liquid crystalline phase. It is possible that the structure of the pure liquid crystalline phase originally formed has been altered in the highly ionic environment. This is also supported by the microscopic examination. The applied electric field during the electrodeposition process can also influence the liquid crystalline structure, although this phase itself is stable at this temperature. The fact that the SEM and STM images show no ordered features on the surface of the porous nickel deposit further confirms that the original liquid crystalline order has been modified in the presence of the nickel deposition constituents. However, what is germane to the present discussion is

that, irrespective of the exact shape of the aggregates in the liquid crystalline phase, a highly porous and crystalline deposit is obtained using this system as a template. The dense distribution of such a large number of nanocrystalline features within and in between the pores as shown by the SEM images of figure 3, is the origin of the high roughness exhibited by this electrodeposited coating of nickel.

3.3.2. X-ray diffraction (XRD) studies

The crystal structure of as deposited porous nickel material was studied by X-ray diffraction analysis. Figures 5 (a-c) show the XRD of bare nickel substrate, the electrodeposited nickel surface from the binary system of water – Triton X-100 (without PAA) and the electrodeposited Ni from the ternary system of water – Triton X-100 – PAA system respectively.

It can be seen from the figure 5 that the X-ray diffraction patterns clearly show the characteristic reflections expected for nickel with face centered cubic (fcc) structure [23]. This also reveals that the resultant nanocrystallites were that of pure fcc nickel. The ratio of intensities of the XRD peaks of 200 and 111 planes for the electrodeposited nickel (without any template), the template-electrodeposited nickel (without PAA) using the binary system and the porous Ni deposit obtained using the ternary system are 1.53, 3.19 and 4.20 respectively. It can be seen that there is a preferential growth of 200 planes for the nickel deposits in the case of template electrodeposition. Table 1 shows the respective values of 2θ, indexing of plane, full width at half maximum (FWHM) and sizes of the nickel nanoparticles obtained from XRD for 111 and 200 planes. We are not showing the results of 220 planes, as its intensity is very much less and therefore associated with a large uncertainty in the measurement of particle size. The average particle size measured for the Ni electrodeposited

material for the two systems (with and without PAA) is 31.6 nm as calculated from the Debye-Scherrer formula shown in the equation (1). The small variation of particle sizes measured using 111 and 200 planes is due to the inherent uncertainty associated with the line broadening method in determining the particle sizes [35]. This result is also supported by the observed nanoscale features of STM image shown in figure 4(b). The fact that the particle sizes of the electrodeposited nickel are almost same for the two specimens obtained using two different systems shows that the template dimensions remain the same in both the cases.

Table-1

XRD analysis of nickel materials obtained using template electrodeposition.

2θ values (deg)	Indexing of planes	Water - Triton X-100 – PAA		Water – Triton X-100	
		FWHM	Particle size (Å)	FWHM	Particle size (Å)
44.6	111	0.2915	294.6	0.2533	339.1
52.0	200	0.2579	342.8	0.3039	291.0

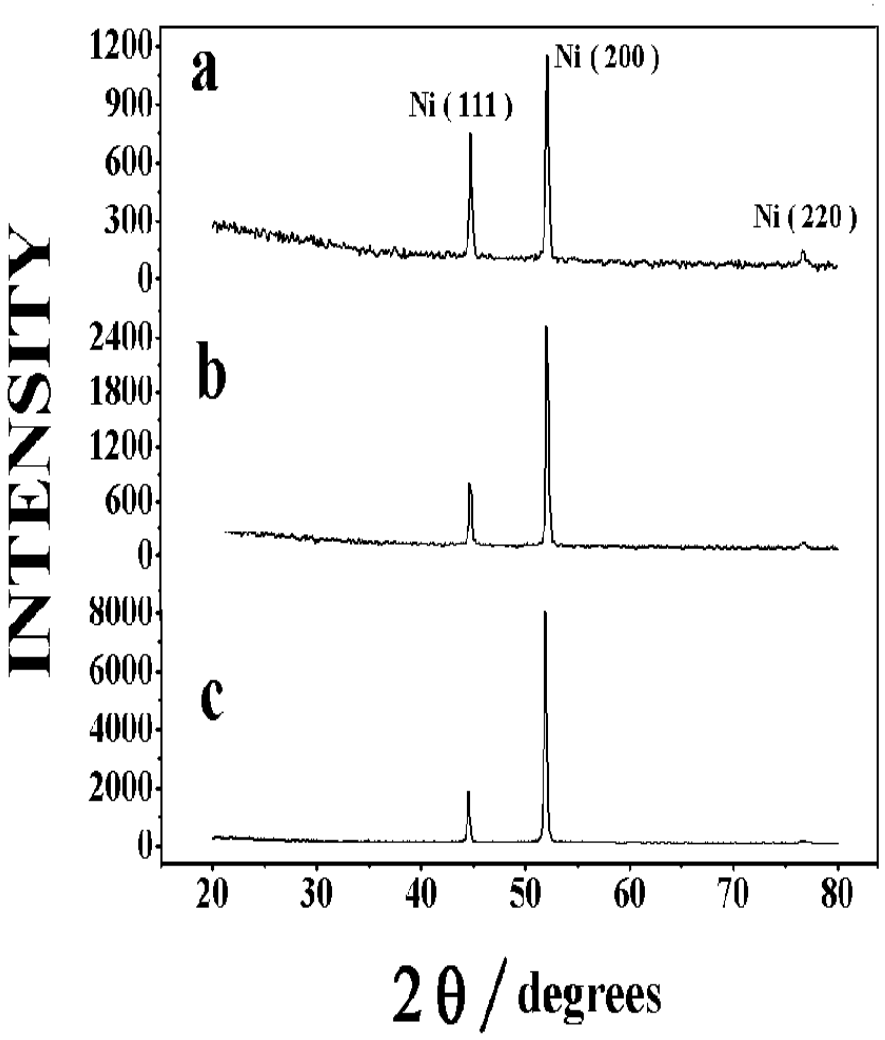

Figure 5: X-ray diffraction pattern of (a) Electrodeposited Ni obtained from nickel sulphamate bath (without any template), (b) Ni electrodeposit obtained using Water - Triton X-100 template (without PAA) and (c) Porous Ni electrodeposit obtained from Water - Triton X-100 - PAA template.

3.3.3. Electrochemical characterization of the porous Ni deposit

We have carried out the template electrodeposition of nickel using a range of current density varying from 2-10 mA/cm^2. Due to the highly resistive nature of the electrolyte, increasing the current density of nickel deposition beyond 10 mA/cm^2 increases the voltage drop across the 2-5 mm gap between the two electrodes leading to a potential overload after a few minutes of electrodeposition. Therefore, the current density for deposition was optimized to 5 mA/cm^2. The as plated nickel is gray-black in appearance. The faradaic current efficiency was estimated to be 55% during the electrodeposition at a current density of 5 mA/cm^2 for about 1hour using the new hexagonal liquid crystalline phase as a template. The thickness of the Ni deposit was measured to be 50μm with a mass of 17 mg/cm^2, showing a porosity of 0.62.

3.3.3.1. Evaluation of porous nickel electrodes as hydrogen evolving cathodes

The porous nickel deposit obtained using the template electrodeposition was evaluated for its applications as a hydrogen-evolving cathode in electrocatalysis. The detailed experimental procedure and the results obtained were discussed in chapter 7. Here we have provided the discussion based on Tafel plot analysis aimed at characterizing the material for hydrogen evolution reaction. The utility of the porous nickel material as hydrogen evolving cathodes has been evaluated electrochemically in 0.5M NaOH aqueous solution. The steady state overpotential (η)–current density (i) data were obtained using chronoamperometry experiments [15,36]. The protocol consisted of first keeping the electrode at a potential of −1.6V vs. SCE for about 5 minutes in the hydrogen evolution region followed by applying a pulse to

−1.02V vs. SCE for 60s to oxidize any hydrides formed on its surface. Finally the desired potential was applied starting from −1.05V vs. SCE to collect the chronoamperometry data. The steady state current is measured at the end of 20s.

Figure 4 shows the linear region of the η vs. log i plots for the smooth as well as the porous nickel electrodes. A Tafel slope of around 120 mV/dec was obtained for both the smooth nickel as well as the electrodeposited high surface area porous nickel electrodes. This indicates that the rate-determining step for the hydrogen evolution reaction is the same in both the cases following the Volmer-Heyrovski mechanism [39-42].

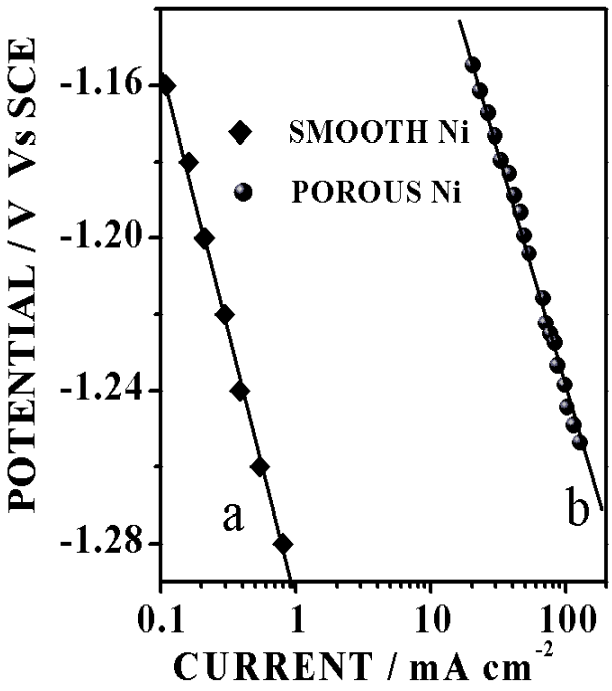

Figure 6: Logarithmic current density vs. potential curves for hydrogen evolution reaction in 0.5M NaOH aqueous solution for, (a) smooth nickel electrode and (b) as plated porous nickel electrode prepared using template electrodeposition.

It can be seen from the figure 6 that there is an increase in current density by more than 200 times due to hydrogen evolution reaction on the porous nickel deposit compared to the smooth nickel electrode. However, whether such an increase is commensurate with the increase in its true surface area has been further investigated using different methods of estimation of true surface area of the gas evolving electrodes. Essentially, the methodology adopted by Rausch et al. [14] and Brown et al. [15] was followed in our analysis. Broadly, we have attempted to evaluate the catalytic activity of the porous nickel by (a) cyclic voltammetric measurement of true electroactive surface area obtained from the anodic charge involved in the formation of a monolayer of $Ni(OH)_2$. (b) electrochemical impedance spectroscopy to determine the double layer capacitance (C_{dl}) of the porous electrodes in the hydrogen evolution region and compare this parameter with that of smooth Ni electrode. This ratio will provide information on the extent of access of the interior portion of the pores to the electrolyte. This is a measure of the electrolytically 'wettable area' during the hydrogen evolution reaction. (c) the chronoamperometric measurement from which the Tafel plots and current density per mass of the material are obtained.

3.3.3.2. Determination of electroactive surface area from cyclic voltammetry

The electroactive surface area (true area) of the porous nickel deposit has been determined by measuring the anodic charge associated with the formation of nickel hydroxide during the cyclic voltammetric measurement in 0.5M NaOH aqueous solution. Figures 7(a) and (b) show the cyclic voltammograms of the smooth polished nickel electrode and the porous nickel deposit respectively when scanned in the potential region where a monolayer of

α-$Ni(OH)_2$ is formed during the anodic scan. This monolayer is stripped off during the reverse scan beyond a potential of –0.9V vs. SCE as can be seen from the oxide-stripping peak [15,36]. However, the CV of porous nickel coating (Fig. 7(b)) shows a rather drawn out oxide formation region signifying a large increase in the true surface area and therefore the overall charge associated with the process. The oxide formation region extends to a potential of –0.2V vs. SCE unlike that of smooth nickel electrode. The reverse peak of oxide stripping is not seen separately as it merges with the large hydrogen evolution current. The charge associated with the formation of a monolayer of α-$Ni(OH)_2$ is known to be 514 $\mu C/cm^2$ [15,36] and an estimation of the area under the anodic peak gives an electroactive true surface area of 652 cm^2. This charge corresponds to a roughness factor value of 3620 in comparison to the roughness factor of 4 obtained for the smooth nickel sample. To the best of our knowledge this is the highest electroactive surface area and the roughness factor for any ***electrodeposited*** nickel reported in literature. It may be pointed out that Rausch and Wendt using the anodic oxidation current measure a roughness factor of 270 for sintered nickel electrode and 12000 for the Raney nickel electrode [14].

We have carried out the deposition of nickel in the triphase system for different time duration. Figure 8 shows a plot of the roughness factor vs. time of deposition for these samples. It can be seen that the roughness factor obtained is maximum for 90 minutes of deposition and does not increase any further with more time. Obviously the growth of porous network that is responsible for the large surface area of the deposited nickel attains a steady state beyond 90 minutes. The average roughness factor of 3 samples obtained after 90 minutes of deposition is 3360. We also find that the temperature of the electroplating

bath containing the hexagonal liquid crystalline phase should be < 27^0C to obtain the high surface area nickel deposit. The nickel deposited at a temperature of above 30^0C produces a surface with very much lower roughness factor of about 240. This is due to the phase transition from the liquid crystalline phase to the isotropic phase above 29^0C, which destroys the template characteristics of the triphase system.

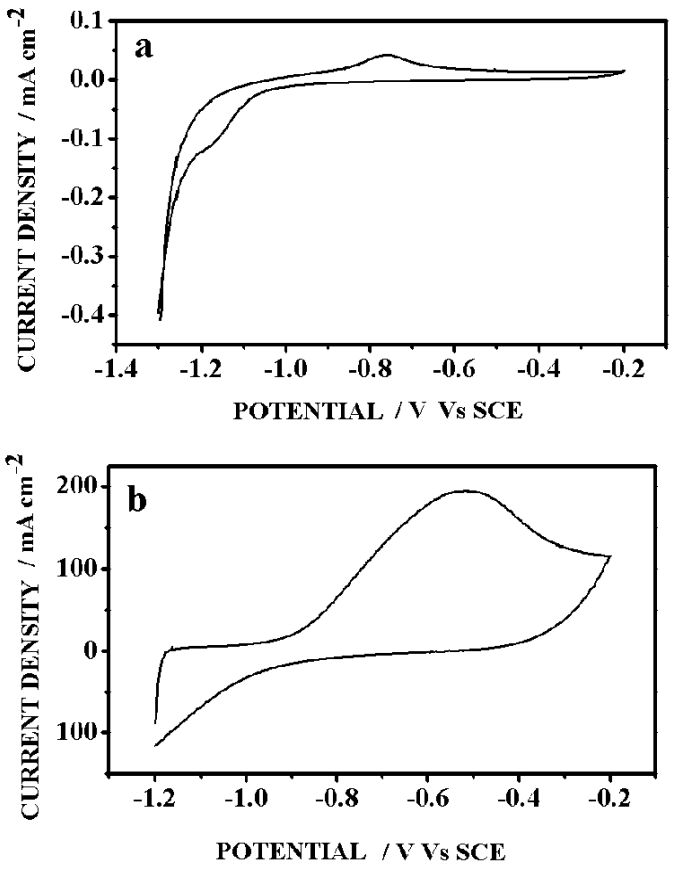

Figure 7: Cyclic voltammograms performed at 50mV/s sweep rate recorded in a 0.5M NaOH aqueous solution for, (a) polished smooth nickel electrode and (b) nickel deposited electrode produced by electroplating at 5 mA/cm^2 current density using a new hexagonal liquid crystalline phase consisting of Water - Triton X-100 - PAA composition.

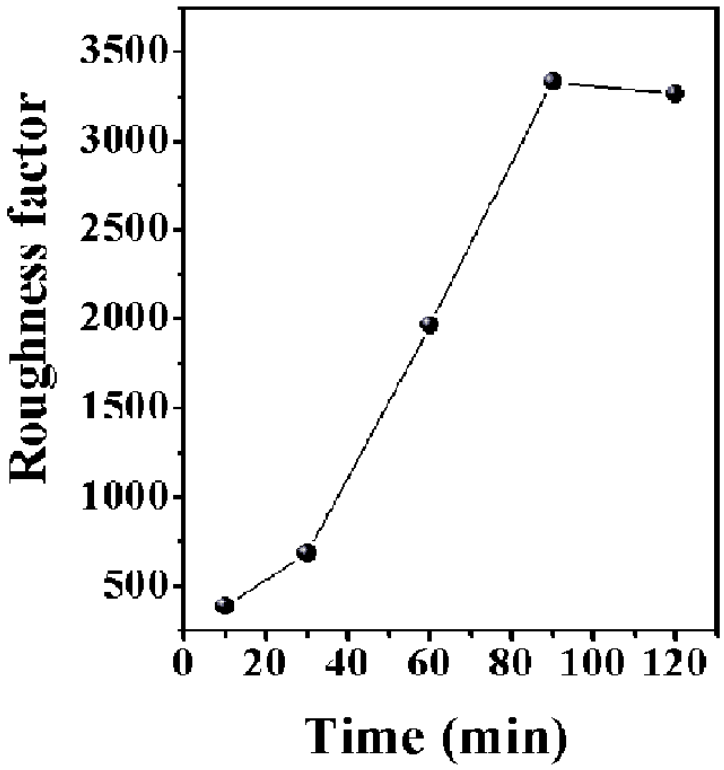

Figure 8: Variation of roughness factor of the porous nickel deposit with time of electroplating using Water - Triton X-100 – PAA system as a template.

It is worth mentioning here that the three-component liquid crystalline phase containing PAA is essential for the preparation of a very high roughness coating. The roughness factor value in the case of template deposition without PAA in the bath composition (water 58% and Triton X-100 42%) was determined to be 435. This is in conformation with the observation using SEM images as can be seen from the figure 3(c) that there is no pore formation in this case unlike the material deposited in water - Triton X-100 - PAA system. This ultimately results in low roughness factor value in the case of binary system when compared to the deposit obtained using the ternary system.

3.3.3.3. Electrochemical impedance spectroscopic studies

We have carried out the electrochemical impedance spectroscopic studies at a potential region between -1.2V and -1.4V vs. SCE for the porous nickel and smooth nickel electrodes in 0.5M NaOH aqueous solution. These studies provide information on the effective surface area available for the hydrogen evolution reaction, which can be used to compare the results with that of the porous nickel prepared using HIPE as a template [15], sintered and Raney nickel electrodes [14]. The Nyquist plots of smooth and porous nickel electrodes at different potential values are shown in the figures 9(a) and (b). We find that the smooth nickel electrode exhibits a single semicircle, which can be fitted to the standard Randle's equivalent circuit comprising of a parallel combination of the charge transfer resistance (R_{ct}) and a double layer capacitance (C_{dl}) with a series solution resistance (R_u). The template deposited porous nickel electrode shows two clear semicircles in the impedance plot. The diameter of the first high frequency arc is potential independent and is quite clearly defined at all the potentials used for the measurement. The second semicircle is potential dependent and the diameter of this semicircle decreases with the overpotential. In addition to this, we observe at high overpotentials a low frequency positive phase angle region corresponding to an inductive element. The low frequency inductive loop for the hydrogen evolution reaction has been earlier proposed by Conway et al. [25] and later experimentally observed by other workers for Ni-Zn [37] and Ni–P [38] alloys in alkaline media. These workers also found a significant absorption of hydrogen and the formation of surface hydride layers in these systems. The reason for the observed inductive behaviour, as can be seen from the figure 9(b), may be due to the hydride formation at these overpotentials, a conclusion that needs to be confirmed by further investigation.

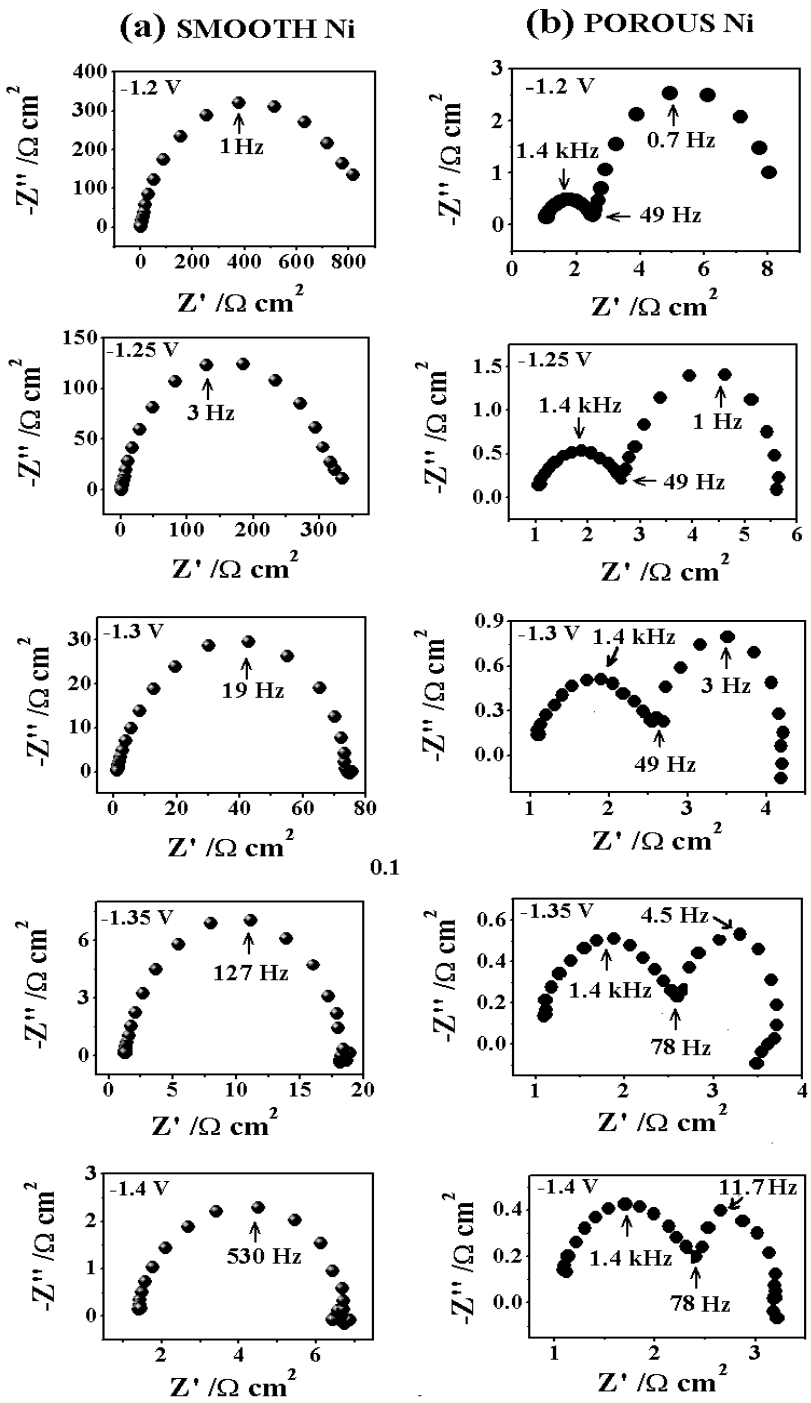

Figure 9: Nyquist plots of polished smooth Ni and porous Ni electrodes in 0.5M NaOH aqueous solution at various potentials in the hydrogen evolution region. Frequency range = 0.1 Hz to 100 kHz. (a) Smooth nickel and (b) Porous nickel electrodes.

The two semicircles obtained in the complex-plane plots having similar characteristics was earlier reported by Lasia et al. [26,27] for the hydrogen evolution reaction on Ni alloy electrodes. They attribute the second semicircle to the kinetics of the charge transfer process and model it to a parallel combination of charge transfer resistance and a double layer capacitance. The higher frequency potential independent first semicircle was ascribed to the surface geometry and pore structure of the electrode. Based on the earlier work of Keiser et al. [31], this behaviour has been discussed for the hydrogen evolution reaction on the porous Ni–Zn and Ni–Al powder electrodes [26,27]. Using digital simulation studies, they model the high frequency depressed semicircle to a solution resistance – double layer capacitance coupling in the pores and derive a flooded pear shaped pore geometry [26,27]. We have carried out the equivalent circuit fitting of the complex plane impedance plot of the porous nickel electrode based on this model. The first semicircle corresponds to a parallel combination of a resistance and a constant phase element (CPE) while the second semicircle arises due to a parallel combination of the charge transfer resistance (R_{ct}) and the double layer capacitance (C_{dl}). These two parallel combinations are in series with each other and with an uncompensated solution resistance, R_u. The porous nature of the surface as shown by the SEM images of the figures 3(a) and (b) and the high frequency potential independent semicircles observed by us strongly suggest that the pores formed in the case of template electrodeposition can be considered to be of flooded pear shaped with a smaller opening and a broader internal structure. The inside conductive region contributes significantly to the overall surface area of the material, which is much larger than the one that can be inferred from the outer surface structure alone.

Figure 10 shows the double layer capacitance values for both the porous and smooth Ni electrodes, obtained by the equivalent circuit fitting analysis, at five different overpotentials at intervals of -50 mV starting from –1.2V vs. SCE. It can be seen that there is a decrease of C_{dl} with the overpotential in both the cases to almost an equal extent. The double layer capacitance of the gas evolving electrodes such as sintered and Raney nickel have been measured and analyzed in detail by Rausch and Wendt [14]. They find that the double layer capacitance decreases with the increasing cathodic overpotential in the case of different nickel electrodes. This effect is attributed to an increasing formation of the gas bubbles at higher overpotentials, which screen the catalytic nickel electrodes and hence the electrochemical accessibility of the electrolyte is prevented. From the ratio of the double layer capacitance of the rough and smooth electrodes these workers calculate the effective working electrode area. Table 2 shows the relative areas as measured by the anodic charge and double layer capacitance measurements for different types of nickel electrodes. It can be noted from the table that for sintered Ni and Raney Ni electrodes, the relative area measured using the double layer capacitance measurement is about 10% of the value obtained from the anodic oxidation charge measurement. This large difference has been attributed to the fraction of the total internal surface effectively accessed by the electrolyte, which is only 10% of the total available area.

It can also be seen from the table 2 that in the case of porous Ni obtained in the present work, the relative area measured by the C_{dl} values is about 530 ± 60 at different potentials used for the study. This can be compared with a value of 905 obtained from the ratio of the roughness factors of porous Ni and smooth Ni electrodes (3620/4) as measured from the anodic oxide charge values. It is clear that almost 58% of the electrode area is electrolytically

accessible for the reaction in the case of porous Ni electrode. The apparent difference in the ratios by a factor of 2 using these two methods can be explained on the basis of the different potential ranges involved in the measurements and the electrochemical processes occurring at these potential ranges. In the case of EIS data, in the hydrogen evolution region, the relative ratio of C_{dl} is lower since certain regions of the surface is not accessible for the electrolyte due to the pore clogging and the surface blanketing by the evolved hydrogen gas. The apparent area measured by C_{dl} is therefore less than the actual true surface area of the material.

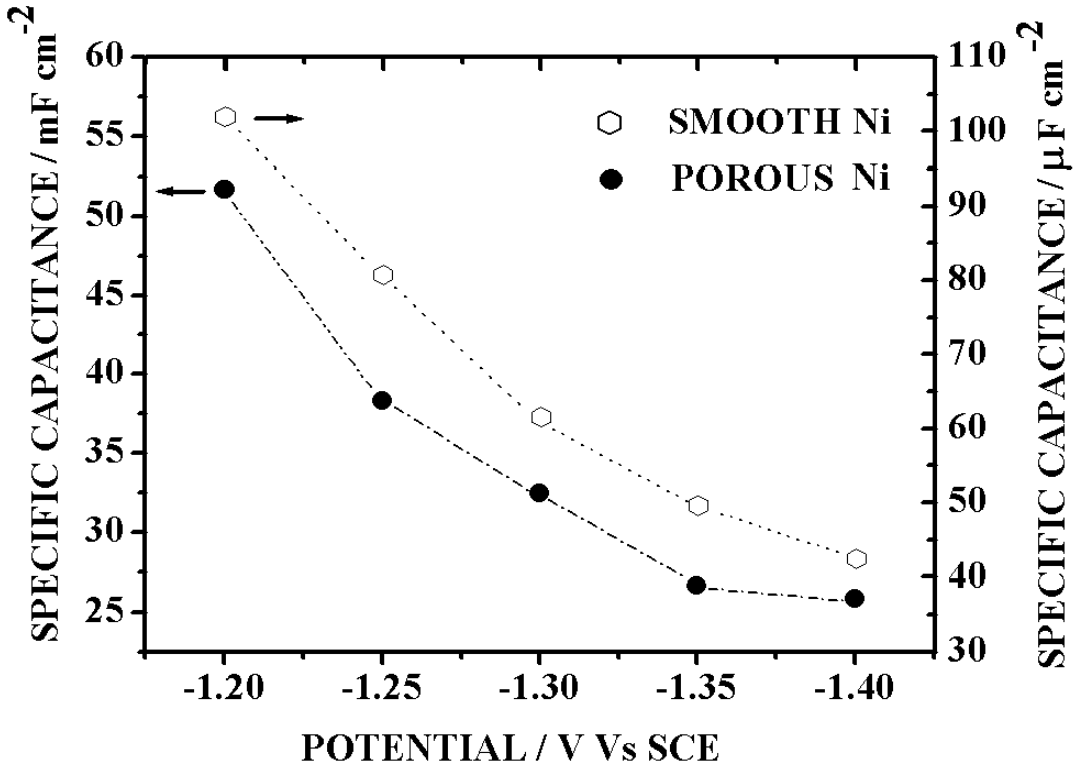

Figure 10: Variation of double layer capacitance (C_{dl}) values with applied potential for the smooth Ni and the porous Ni electrodes measured in 0.5M NaOH aqueous solution. The lines connecting the points are drawn as aid to the eyes.

Table-2

The relative effective nickel electrode area as measured by anodic oxidation charge, double layer capacitance and hydrogen evolution current ratios of different nickel electrodes and a smooth reference nickel surface.

Method	Smooth nickel	Sintered nickel (Ref. [14], Table 1)	Raney nickel (Ref. [14], Table 1)	Porous nickel (HIPE Template prepared at 50 mA/cm^2, Ref. [15])	Porous nickel (Present work)
Anodic oxidation	**1**	**270**	**12000**	**66[a]**	**905[b]**
Double layer capacitance	**1**	**33**	**1200**	**No data available**	**530 ± 60**
Current potential curves	**1**	**50**	**34 (at 1 mA/cm^2) 1000 (at 1 A/cm^2)**	**65[c]**	**230**

Note:

a. Compared to roughness factor of smooth Ni = 1.3 as per Table 1, Reference 15.

b. Compared to roughness factor of smooth Ni = 4 in the present work.

c. Value extracted from Figure 4 (a), Reference 15.

From the analysis of results obtained using the electrochemical characterization techniques, it is clear that the porous nickel material prepared using the present liquid crystalline template shows the most effective utilization of the available surface area for the hydrogen evolution reaction. The effectiveness of the material arises essentially due to a very large electroactive

surface area, which is also quite well accessed by the electrolyte, as shown by our double layer capacitance results. This clearly shows that the high surface area porous Ni has the potential to be used as a hydrogen-evolving cathode in electrocatalysis.

The large surface area value obtained for this porous nickel using the electrochemical measurements can be compared with the surface area ratio parameter of 140 measured using STM. If it is assumed that the surfaces scanned are the representative of the entire surface at this length scale, then the measured roughness factor using STM surface profiling is lower than the electrochemically active true surface area of 380 for 10 minutes deposited nickel electrode that has been used for the STM studies. Therefore, it is concluded that the higher surface area measured by the electrochemical method arises essentially due to the contribution of nanoscale particles within the side walls of the extensively distributed pores. This is also in conformity with our earlier conclusion based on EIS equivalent circuit modeling, which points to the flooded pear shaped pore formation and large internal area contributing significantly to the measured true surface area. It may be mentioned here that the STM image is obtained on a porous nickel electrodeposited on gold on mica substrate. The fact that the microcrystalline structural features of the porous nickel remains the same for a surface deposited for 60 minutes as seen from the SEM picture shown in figure 3(b) shows that the nucleation and growth of these particles is more or less uniform throughout the process of deposition and is not significantly affected by the thickness of the coating.

3.3.3.4. Nickel electrode as a double layer capacitor

We have evaluated the high surface area porous nickel electrode for its potential application as a supercapacitor electrode material. There have been

several reports on nickel oxide being used as a supercapacitor electrode material [16-19]. Electrochemical precipitation of $Ni(OH)_2$ followed by heating at various temperatures to obtain nickel oxide has been reported earlier [16-18]. The high capacitance value obtained for this material has been attributed to increase in the surface area [16,17] as well as to the non-stoichiometric nature of the nickel oxide electrode material [18].

Figure 11(a) shows the cyclic voltammogram of as plated porous nickel in the nickel oxide region in 0.5M NaOH aqueous solution when it is scanned from –0.1V to +0.5V vs. SCE at 50 mV/s for about 25 cycles. This is to produce a clean activated surface [16-19]. It can be seen from the figure that the oxide formation occurs at a potential more positive to +0.25V vs. SCE while the reverse peak formation is due to stripping of nickel oxide. To measure the capacitance of the nickel electrode, we have chosen a potential range between –0.1V and +0.25V vs. SCE as in this region no redox reaction occurs [18].

Figure 11(b) shows the cyclic voltammogram of template-electrodeposited nickel in the reduced potential range from –0.1V to +0.25V vs. SCE in 0.5M NaOH aqueous solution at 50 mV/s scan rate at the end of 25 cycles. The CV shows a familiar rectangular box shape as expected for ideal capacitors. The single electrode capacitance value of 338 mF/cm^2 and a capacitance per unit mass of 50 F/g determined for as plated nickel electrode shows that this can be a useful material in electrochemical capacitors. It is worth pointing out that the preparation of this material does not require any post thermal treatment after the electrodeposition to obtain nickel oxide as previously reported in the literature [16-18]. We find that the surface has an intense black colour after scanning in the nickel oxide (NiO) region.

From these experimental results, it is clear that the mass transfer plays a vital role in the template electrodeposition. In this connection, we also

observe an increase in the mass transfer by the application of external magnetic field during the process of electrolysis of nickel that affects the structural morphology and the properties of nickel deposit. A detailed study of this phenomenon has been described in the following section.

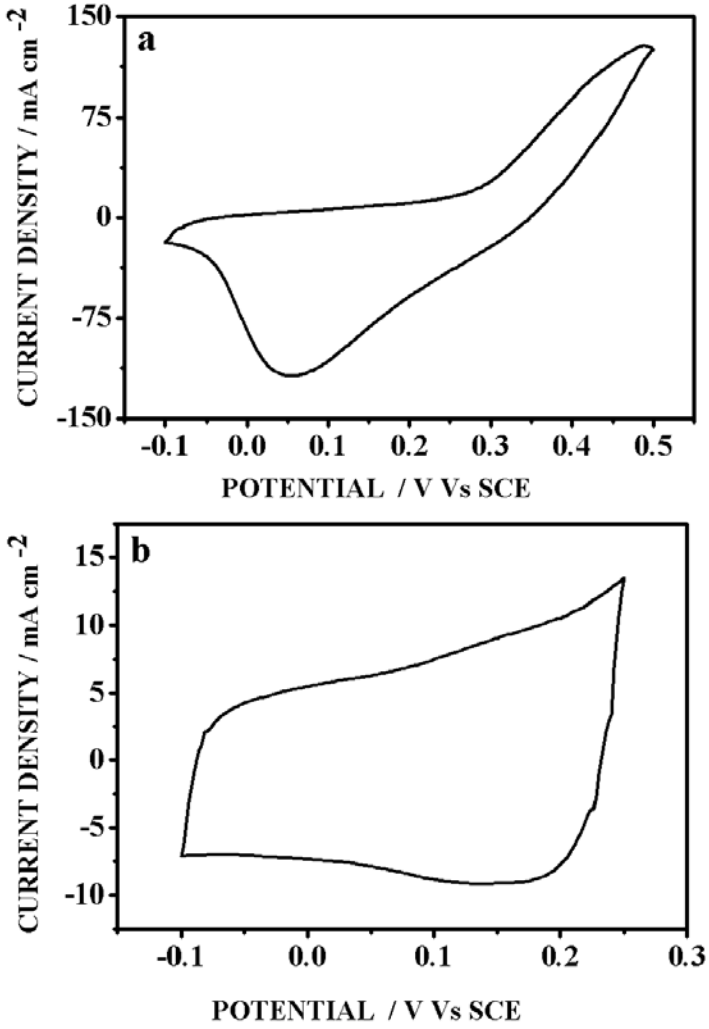

Figure 11: (a) Cyclic voltammogram of as plated porous nickel electrode in 0.5M NaOH aqueous solution after 25 cycles. (b) Cyclic voltammogram of the porous nickel electrode in 0.5M NaOH aqueous solution in the reduced potential range after 25 cycles. Sweep rate: 50 mV/s.

II. EFFECT OF APPLIED MAGNETIC FIELD ON THE ELECTRODEPOSITION OF NICKEL

3.4. Introduction

We have carried out the experimental work to study the effect of applied magnetic field on the electrodeposition of nickel and the influence of mass transfer on the structural morphology of the nickel deposit. The deposition of a metal or an alloy by electric current in the presence of an applied magnetic field is known as magnetoelectrolysis (ME) [43-45] or magneto electrolytic deposition. There have been several attempts to investigate the effect of imposed magnetic field on the electrolyte properties, electrolytic mass transport and to some extent on the electrode kinetics. Normally the effects due to magnetic field are studied by investigating the structure and morphology of the deposit by applying an external magnetic field in parallel and perpendicular directions during the process of electrolysis. Many of the metals and its alloys such as nickel, silver, copper and zinc, prepared by electrodeposition in the presence of a magnetic field had been examined for their structural and morphological properties using various surface characterization techniques. For example, it was observed that the dendritic growth of zinc or lead can be strongly modified by imposing an external magnetic field and in some cases the dendritic growth may be totally inhibited due to an increase in the rate of metal deposition resulting in a smooth deposit [46,47].

Hinds et al. [48,49] reported that the mass transfer controlled deposition current is almost doubled on applying an external magnetic field of 0.6T in the case of copper magnetoelectrolysis and observed that the process is independent of field direction and electrode orientation [48]. A complete analysis of magnetic field effects on copper electrolysis based on electrochemical techniques had also been reported. The increase in the rate of

mass transport was attributed to the formation of a hydrodynamic boundary layer at the electrode surface due to the tangential velocity induced by the field that actually decreases the diffusion layer thickness and increases the flux of the species [49]. Coey and Hinds [50] reported that the magnetic fields could be used during electrodeposition to enhance the deposition rate of magnetic species and also to induce turbulent flow. They found that the morphology of radially grown electrodeposits is very much sensitive to the applied magnetic field.

The observed results in almost all the above cases had been attributed to the magnetohydrodynamic (MHD) effect, which arises from the Lorentz force, due to the interaction of velocity fields of charged species with the electromagnetic fields. The total force on a charged particle like electron or an ion, moving in an electromagnetic field is the Lorentz force and it is given by,

$$\mathbf{F_L} = q\,(\mathbf{E} + \mathbf{v} \times \mathbf{B}) \qquad (2)$$

where $\mathbf{F_L}$ is the Lorentz force, q the charge of an ion, **E** the electric field strength, **v** the velocity of the ions and **B** the magnetic flux density.

When a magnetic field is applied parallel to the deposit plane of an electrode surface (i.e. perpendicular to the direction of flow of ions under the electric field), the Lorentz force is exerted on the moving ions which are the charge carriers in the electrolyte and thereby induces a convective flow of the electrolytic solution. This process increases the mass transport effect and significantly affects the usual consequences of diffusion-controlled processes. This magnetically induced convection reduces the thickness of the Nernst diffusion layer thereby enhancing the limiting current density I_L. The effect of MHD on mass transport is usually studied by measuring the limiting current density (I_L) of various electrochemical processes. There are several empirical relationships reported for the dependence of I_L on the magnetic flux density B

[51-53], though it is now generally accepted that I_L is proportional to $\mathbf{B}^{1/3}$ [49,54].

In addition to the Lorentz force, the forced convection due to magnetic field can also arise in an electrolyte in which a concentration gradient of the paramagnetic ions can exist due to some redox reaction in which they participate. This gradient generates the regions of varying magnetic susceptibility that is subjected to a force by the applied external field. This force which has the same vector as the velocity of the moving ions in the electric field will generate a convective transport of all the components of the solution [55] which in turn will affect the mass transfer and hence I_L. However there have been conflicting views on the extent of the influence of this force on the convective flow of the electrolyte in literature [49,56].

There have been a several reports in the literature on the effect of a magnetic field on the electrodeposition of nickel [57-65]. Based on the reflection high-energy electron diffraction (RHEED) study of Ni, Fe and Co, Yang reported that an imposed magnetic field had little effect on their preferred orientations of growth during electrodeposition. But an increase in the roughness of the deposit with projections protruding in the direction of the applied perpendicular magnetic field was observed [57]. On the contrary, Perakh reported a large difference in macro-stresses for nickel and iron-nickel alloy films due to a magnetic field applied parallel to the substrate [58]. Chiba et al. [59] using X-ray diffraction (XRD) analysis concluded that the magnetic field could modify the crystal growth orientations in relation to the easy magnetization axis and this effect is more dominant at low current densities where the magnetic field effect dominates over the electric field.

Shannon et al. [60,61] by means of confocal scanning laser microscopy (CSLM) investigated the effect of both the horizontal and vertical imposed

magnetic fields on the surface roughness of cathodic nickel deposits. Based on the surface depth profile analysis and Bartlett's test of homogeneity, these authors reported that the deposit roughness depends strongly on relative position within the deposit surface and the orientation of applied magnetic field. In general magnetoelectrolysis process leads to a smoother surface compared to the deposition in the absence of magnetic field. Brillas et al. [62,63] found that the imposition of an external magnetic field on nickel electrodeposition, either parallel or perpendicular to the electrodes, leads to an enhancement in the compactness of nickel grains, which grow with more regular sizes and geometrical shapes and concluded that the surface morphology was greatly influenced by the applied magnetic field.

Using scanning electron microscopy (SEM) and transmission electron microscopy (TEM) techniques, Devos et al. [64,65] observed some surface morphological changes with modifications on the preferential growth direction of nickel grains when a magnetic field was applied parallel to the substrate during nickel electrodeposition. These authors attributed the changes to increase in the diffusion flux of certain species such as H^+ in a pure Watts bath or 2-butyne-1,4-diol in modified Watts solution. The reduction of these species on the cathode surface leads to a small increase in the interfacial pH value, thus generating the nickel hydroxide formation in the close vicinity of the surface. This adsorbed species hindered the active part of the cathode surface for nickel electrodeposition that leads to a weak decrease in the electrolysis current density with the increase in the applied magnetic field. This had also been proved by electrochemical characterization techniques.

Recently, Bund et al. [56] investigated the influence of a perpendicular magnetic field on the electrochemical behaviour of Cu, Ni and $[IrCl_6]^{2-|3-}$ systems. The increase of limiting current density with the magnetic field had

been explained based on the increase in the convection flow due to MHD effect. Observation of the formation of more fine-grained material in the presence of a perpendicular magnetic field in the case of nickel electrodeposition had been attributed to increased convection current that leads to an increase in the deposition rate.

The studies on the effect of applied magnetic field on the electrochemical processes are normally carried out with the magnetic field being applied parallel to the electrode surface as at this orientation the MHD force is maximum. If it is desired to eliminate the convection due to MHD and study the paramagnetic force and field gradient effects, then the magnetic field is applied perpendicular to the electrode surface. In this work, we have studied the effect of an externally imposed magnetic field at an angle of 45^0 to the cathodic surface on nickel electrodeposition. We were interested in studying the effect of the orientation of magnetic field at this angle on the surface morphology and deposit properties and the mass transfer process. Such a study carried out with nickel in the presence of nickel ion electrolyte will also provide information on the effect of the applied magnetic field on the ferromagnetic electrode–solution interface.

The magnetically electrodeposited material has been characterized using surface techniques such as scanning electron microscopy (SEM), scanning tunneling microscopy (STM) and X-ray diffraction (XRD). The electrochemical techniques, namely chronopotentiometry and cyclic voltammetry (CV) have been used to monitor the growth process of the deposit and later to characterize the roughness factor of the nickel deposit quantitatively. Electrochemical impedance spectroscopy and Tafel plot analysis have been performed to study the hydrogen evolution reaction on the nickel surface prepared by the process of magnetoelectrolysis.

3.5. Experimental section

3.5.1. Chemicals

Nickel (II) chloride (EMerck), nickel sulphamate (Grauer and Wheel), boric acid (Sarabhai chemicals), sodium hydroxide pellets (Emerck) were used in this study. All the chemical reagents used were AnalaR (AR) grade. Millipore water having a resistivity of 18 MΩ cm was used in all the experiments.

3.5.2. Nickel electroplating in the presence of a magnetic field

For nickel electrodeposition, we have used the standard nickel sulphamate bath [21] described earlier having the composition: 300 g/l nickel sulphamate, 6 g/l nickel chloride and 30 g/l boric acid. The nickel substrates having the typical size of 1mm x 5mm x 5mm were used as strips for electrodeposition. The experimental setup used for the magnetoelectrolysis of nickel is shown in figure 12. A three-electrode cell made up of PTFE (Teflon) was used for the electrodeposition of nickel in the presence of an external magnetic field. The electrical wires are taken through a long stainless steel tube and the top end of which is hermetically sealed. The cell was introduced in the 14 mm bore of a split pair 7 Tesla superconducting magnet (Oxford Instruments, UK) with a built-in variable temperature liquid helium cryostat. A large surface area platinum foil was used as a counter electrode and a silver rod was used as a quasi-reference electrode with nickel strips being used as a working electrode containing a total cell volume of 5cc of nickel solution. The distance between the nickel strip and the platinum foil is about 2-5 mm. A magnetic field of 1Tesla at angle of 45^0 to the nickel strip was applied and the cell temperature was maintained at 25^0C. The magneto electrolysis was carried out at a current density of 10 mA/cm^2 at 25^0C for about 1hour. Before

electroplating, the nickel strips were activated by immersion into a solution of 1:1 HCl in water for a few seconds. The platinum foil was cleaned in conc. HNO_3 acid and the silver rod in dil. HNO_3 acid for a few seconds. The electrodeposited specimen were washed thoroughly with distilled water and then rinsed with millipore water and immediately used for the analysis. For comparison, nickel electrodeposition in the absence of a magnetic field was also performed in the same cell geometry and at the same current density. The magnetoelectrolysis of nickel was carried out in galvanostatic (at constant current density) mode and the potential during the deposition was monitored using chronopotentiometry.

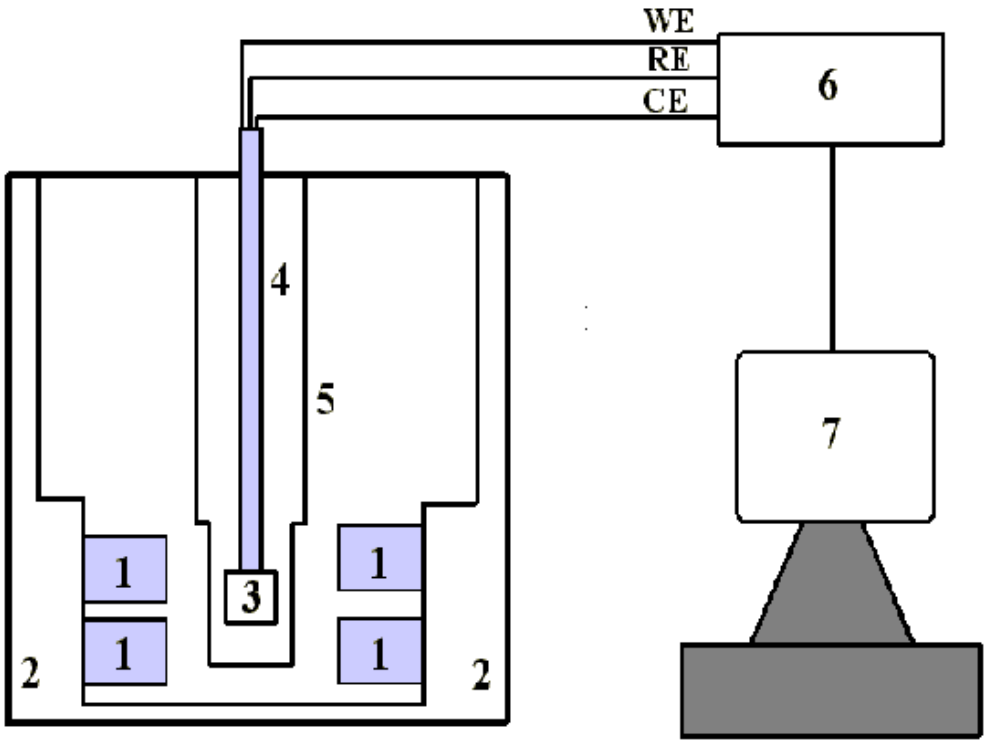

Figure 12: Schematic diagram of the experimental setup used for the magnetoelectrolysis of nickel: (1) Superconducting magnet; (2) Liquid nitrogen bath; (3) Electrochemical cell; (4) Stainless steel tube; (5) Cryostat; (6) Potentiostat; (7) Personal computer (PC).

3.5.3. Characterization of nickel coated electrodes

The SEM characterization of the electrodeposited material has been done using JEOL JSM-840A model instrument and the measurement parameters have been shown in the respective diagrams. Scanning tunneling microscopic studies have been carried out using a home-built instrument [22] with an electrochemically etched tungsten tip as a probe. The images were obtained under the constant current mode at a tunneling current of 1nA and a substrate bias voltage of +100 mV. The roughness analysis of the STM data was performed using SPIP software (Image Metrology, Denmark). The STM was calibrated using a highly oriented pyrolytic graphite (HOPG) sample before carrying out the measurements.

X-ray diffraction measurements were conducted in a SHIMADZU X-ray diffractometer using Cu-Kα radiation having a wavelength of 1.540 A^0. The 2θ value is varied from 20 to 80 degrees. The size of the particle is calculated from the full width at half maximum (FWHM) of the respective peak using Debye-Scherrer equation [23,24], which is shown in the equation (1).

Electrochemical characterization of the nickel deposit was carried out in an all glass three-electrode electrochemical cell. A platinum foil of large surface area was used as a counter electrode and a saturated calomel electrode (SCE) as a reference electrode. Cyclic voltammetry was performed in the potential range from -1.2V to -0.2V vs. SCE in 0.5M NaOH aqueous solution at a potential scan rate of 50 mV/s. Before the beginning of the experiments, the nickel electrode was maintained at a potential of -1.6V vs. SCE for 600s in 0.5M NaOH aqueous solution. This process reduces the surface oxides present on the nickel electrode and cathodically cleans the surface by the evolution of hydrogen gas. This is followed by keeping the nickel electrode at a potential of -1.02V vs. SCE in order to oxidize any metal hydrides present on the surface.

Then finally the potential is scanned from -1.2V to -0.2V vs. SCE to obtain the nickel oxidation and reduction characteristics from which the roughness factor is determined [15]. The chronoamperometric experiments for hydrogen evolution reaction were conducted by the application of a series of potential steps of 10 mV amplitude for a duration of 20s between –1.1V to –1.4V vs. SCE in a cell containing a separate compartment for the reference electrode. The potential data were corrected for ohmic drop due to the solution resistance R_u, determined using current interruption technique. The electrochemical impedance spectroscopic measurements were performed in the hydrogen evolution region at different potentials at a potential interval of 50 mV between –1.2V and –1.4V vs. SCE. EIS data were used to understand the hydrogen evolution reaction on the nickel surface obtained by magneto electrolytic deposition.

The cyclic voltammetric studies were performed using an EG&G potentiostat (model 263A) interfaced to the computer through a GPIB card (National Instruments).

3.6. Results and discussion

3.6.1. Characterization of nickel deposit using SEM and STM

Figure 13(a) shows the SEM image of the nickel surface electrodeposited at 10 mA/cm^2 current density for about 1hour using nickel sulphamate bath in the absence of a magnetic field. A regular uniform layer type growth of nickel deposit has been observed. The surface, though macroscopically smooth, contains several irregular domains having the microscale roughness.

Figure 13(b) shows the SEM picture of the nickel deposit obtained by electroplating at 10 mA/cm^2 current density in the presence of an applied

magnetic field of 1Tesla. It can be seen that the nickel deposit contains several large domains of 1-2μm in size, which in turn are made up of smaller domains. In addition, the tiny spherical particles of 100 nm – 300 nm in diameter are formed on the top layer of the deposit and these particles are mainly concentrated at the grain boundary region of the surface.

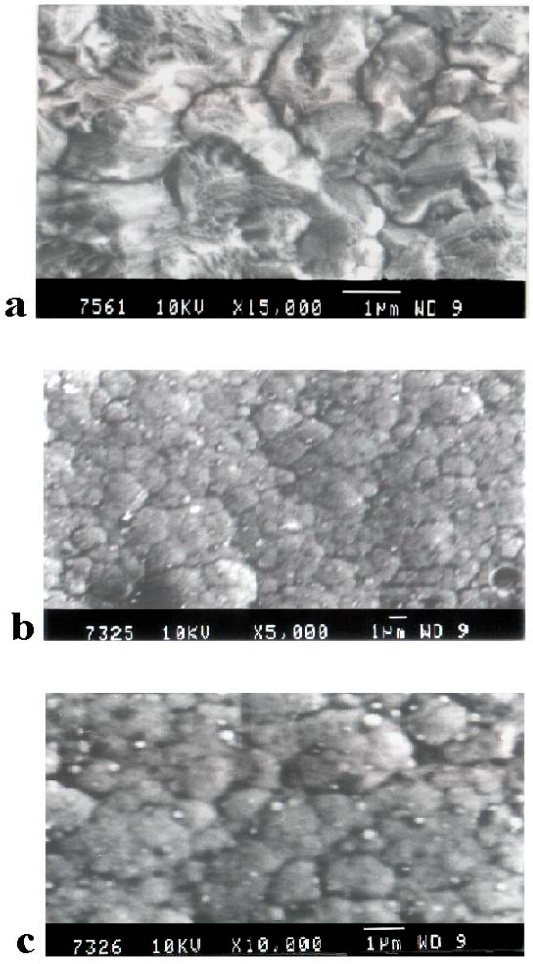

Figure 13: SEM micrographs of nickel electrodeposits obtained at 10 mA/cm^2 current density for 1hour deposition: (a) in the absence of a magnetic field, (b) in the presence of a magnetic field of 1Tesla and (c) same as (b) but with higher magnification showing the formation of spherical nanoparticles at domain boundaries. The other parameters are shown in the respective diagrams.

Figure 13(c) shows a higher magnification image of the nickel deposit obtained in the presence of a magnetic field. This clearly shows the formation of domains of nickel of approximately one micron in size. The nickel nanoparticles are found at the domain boundaries and it is distributed uniformly throughout the surface. The sizes of these nanoparticles vary from ~100 nm - 300 nm. A closer examination of the images suggests that the domains are actually made up of clusters of nickel nanoparticles that agglomerate with each other to form the big domains. This shows that the fresh nucleation and growth of these particles take place predominantly at the domain boundaries, which subsequently aggregate to form the bigger domains.

The above results show that the nickel deposit is fine grained and the process of electrodeposition in the presence of applied magnetic field at the current density of 10 mA/cm^2 assists the fresh nucleation and growth process. Our results can be compared with that of Devos et al. [64] who have studied the nickel electrodeposition in an organic inhibitor containing Watts bath under the applied magnetic field of 0.9T parallel to the surface where they find significant grain size reduction from 2μm to 0.07μm. However, no significant morphological changes were observed when the deposition was carried out using pure Watts bath. This has been explained based on the increased convective flow of the inhibitor species in the modified Watts bath due to MHD effect. Shannon et al. [60] find that the nickel deposit becomes smoother with the increasing magnetic field that has been applied perpendicular to the cathode surface. In contrast, when the magnetic field was applied parallel to the surface, the deposit smoothness increases with decreasing flux density. Bund et al. [56] characterized the nickel deposit prepared using Watts bath and report a fine grain deposit in the presence of magnetic field applied parallel to the surface. They attribute this to increase in the deposition rate due to the convection

brought about by both the MHD effect and the paramagnetic forces. It is worth noting that in all the above cases the Ni deposit obtained has smoother texture when prepared under a magnetic field applied parallel to the surface where the Lorentz force is maximum. Our results show that at an angle of 45^0 the nickel surface obtained is still smooth and fine grained which is clear from the SEM images.

Figure 14(a) shows the STM image of the electrodeposited nickel surface in the absence of a magnetic field. The surface shows a smooth structure with steps of step height of tens of nanometers and terraces of width extending to about 500nm. Figures 14 (b) and (c) show the STM images of nickel surface obtained by electrodeposition in the presence of a magnetic field of 1Tesla. The domains of nickel nanoparticles with a size ranging from 0.6μm – 0.8μm can be clearly seen confirming the similar image obtained using SEM. At smaller ranges, the deposit shows several nanoparticles of size ranging from 20 nm to 25nm. These domains are rather flat and elongated in one direction. These nanometer size domains further aggregate to form the bigger domains, which are generally spherical in shape. From the STM images, it is clear that the electrodeposition in the presence of a magnetic field produces fine-grained structure unlike the smooth terraces obtained in the absence of magnetic field. Similar kind of structural changes of the deposit in the presence of applied magnetic field was reported by Matsushima et al. for the case of iron electrodeposition using atomic force microscopy (AFM) [66]. They observed angular shaped structure when no magnetic field was applied and roundish iron grains when it is deposited in the presence of an applied magnetic field.

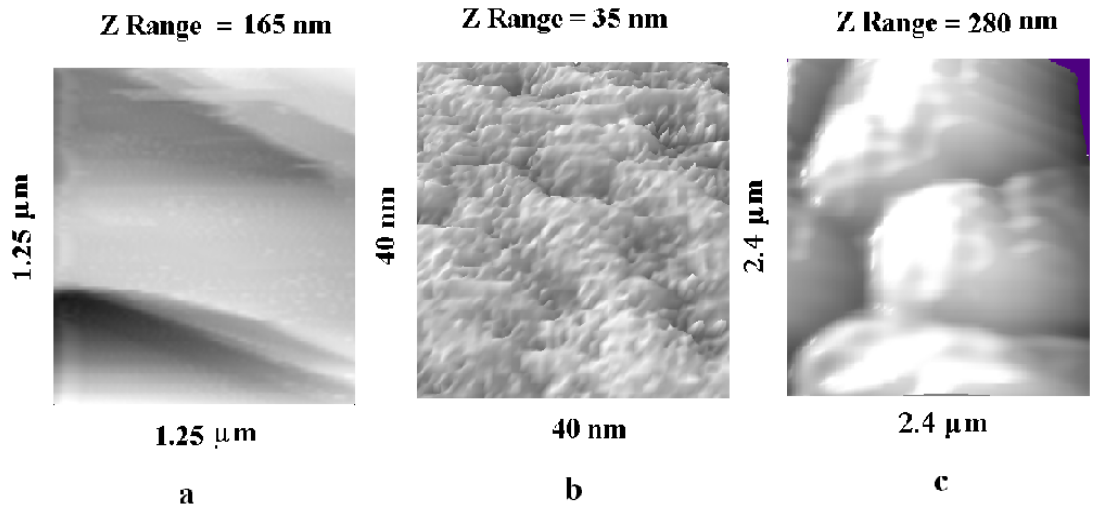

Figure 14: Constant current STM images: Tunneling current: 1nA, Bias voltage: Sample +100 mV. (a) Nickel surface produced by electrodeposition in the absence of a magnetic field. Scan range: 1.25μm x 1.25 μm. (b) Scan range: 40nm x 40nm. (c) Scan range: 2.4μm x 2.4μm for an electroplated nickel in the presence of a magnetic field of 1 Tesla.

3.6.2. X-ray diffraction (XRD) studies

The crystal structure of the as deposited nickel nanoparticles was studied using X-ray diffraction analysis. Figures 15 (a) and (b) show respectively the XRD of bare nickel substrate in the absence of a magnetic field and electrodeposited nickel in the presence of a magnetic field of 1Tesla at a current density of 10 mA/cm^2 for about 1hour.

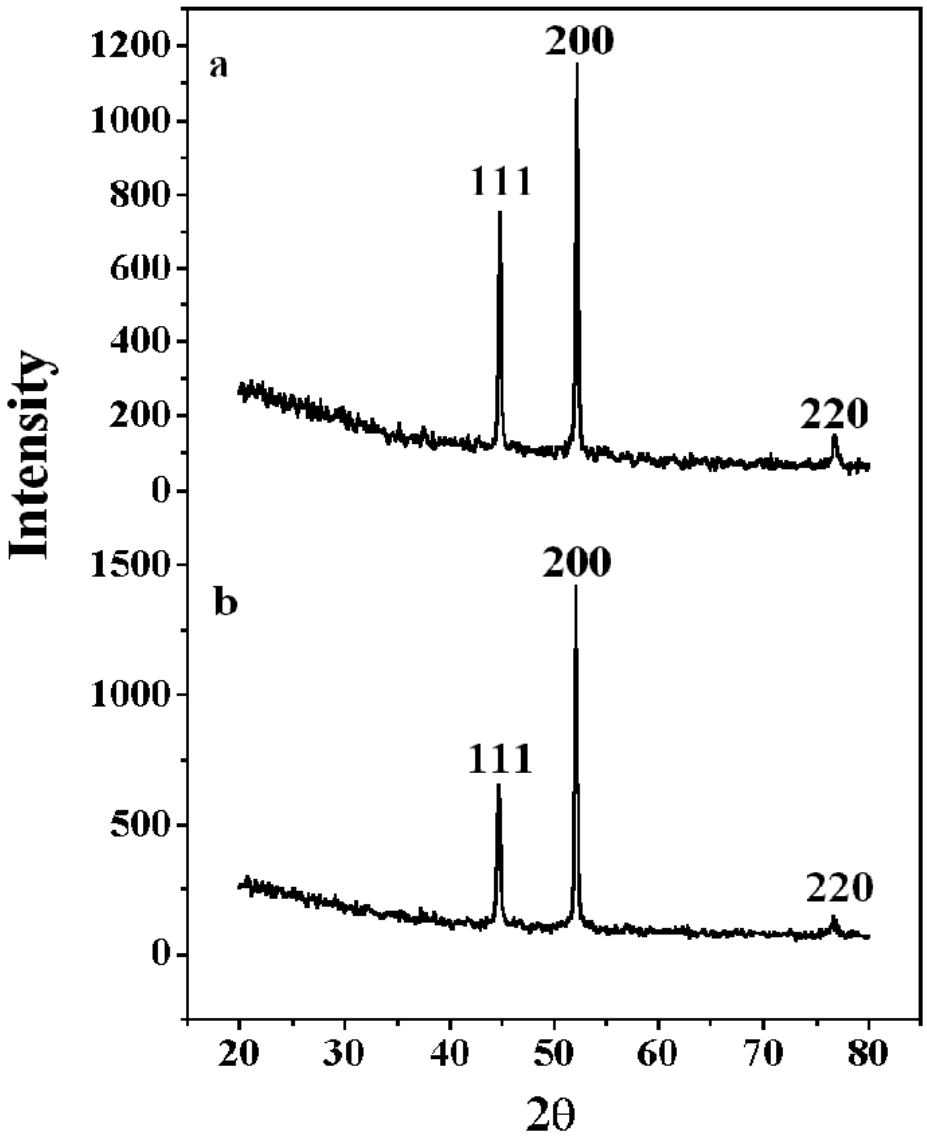

Figure 15: X-ray diffraction spectra of: (a) electrodeposited nickel in the absence of a magnetic field and (b) electrodeposited nickel in the presence of a magnetic field of 1Tesla.

The X-ray diffraction patterns clearly show the characteristic reflections expected for nickel with face centered cubic (fcc) structure [23]. Table 3 shows the respective values of 2θ, indexing of plane, full width at half maximum (FWHM) and sizes of the nanoparticles determined from XRD studies. The particle size is measured to be ~17-18 nm as calculated from the Debye-Scherrer equation (1). It can be seen from the XRD pattern, that while the 111 planes are still the predominant orientation, there is an increase in the intensity of 200 planes in the case of nickel deposited under a magnetic field of 1Tesla. Brillas et al. [62] have studied the effect of 0.9T magnetic field on the crystallographic orientation of nickel using X-ray diffraction technique. The preferred orientation of the crystal planes of nickel deposited under the magnetic field however was dependent on the electroplating bath used and the current density employed for the deposition. For instance, the 111 plane is the predominant plane for the nickel deposited in Watts bath under both the parallel and perpendicular orientation of the magnetic field. Though we find that nickel deposited in sulphamate bath shows predominance of 111 plane, there is a significant increase in the intensity of 200 plane under the applied magnetic field at 45^0 angle orientation. This shows that though the predominant orientation is still dictated by the electric field, the magnetic field begins to exert its influence in the crystallographic orientation at an applied field of 1Tesla. This is similar to the effect observed by Matsushima et al. [66] who found that the predominant preferred orientation of 211 plane for iron is retained in the presence of magnetic field though with slightly decreased intensity while the intensity of 110 plane is increased slightly. It is quite conceivable for the ferromagnetic metals such as nickel the induced magnetic dipolar effects can have significant influence on the growth morphology [67].

Table-3

XRD analysis of electrodeposited nickel obtained in the presence of a magnetic field of 1Tesla.

2θ values (deg)	Indexing of planes	FWHM	Particle size (A^0)
44.6	111	0.49965	172
52.0	200	0.50886	174

3.6.3. Electrochemical characterization

The electrodeposition of nickel in the presence of a magnetic field of 1Tesla at an angle of 45^0 to the cathode surface has been carried out at a constant current density of 10 mA/cm^2. The change in potential with time during the magnetoelectrolysis of nickel was monitored using chronopotentiometry. After the electrodeposition, the specimens obtained both in the presence and absence of magnetic field were characterized using cyclic voltammetry in order to determine the roughness factor values. We have also carried out Tafel plot analysis in order to study the hydrogen evolution reaction on nickel surface prepared using magnetoelectrolysis.

3.6.3.1. Chronopotentiometry

The change of potential with time during the electrodeposition of nickel at 10 mA/cm^2 current density in the absence and in the presence of magnetic field are shown in the figures 16 (a) and (b) respectively. There are two important points that can be observed from these figures and it is worth

noting. One is the large shift in the rest potential of the nickel electrode in the electrolyte on the application of a magnetic field and the other point is decrease of overpotential with time once the electrolysis begins.

It can be seen from the figure 16(b) that the rest potential of the nickel electrode is shifted from –25 mV vs. Ag reference electrode in the absence of magnetic field to –440 mV on the application of 1Tesla magnetic field. Similar large shift in the electrode rest potential has been earlier observed by Matsushima et al. [66] for iron electrode in an electrolyte containing ferrous ions. We feel that the shift in the electrode potential arises due to the field induced shift in chemical potential of Ni electrode and any ferromagnetic electrode in general as suggested by Shimada et al. [68]. According to these workers, for ferromagnetic metals under the influence of magnetic field, owing to the difference in the density of states (DOS) of electrons of opposite spins in the Fermi energy levels, there is a shift in the chemical potential of the whole electron system. The shift in chemical potential manifests as a shift in the electrode potential of the electrode–solution interface.

In addition to this shift in the electrode potential there is a significant decrease of overpotential with time in the presence of a magnetic field. In the normal nickel electrodeposition without any magnetic field, the overpotential immediately on the application of a current density of 10 mA/cm^2 at t = 0 is –730 mV which during the 1hour deposition time decreases to –680 mV as can be seen from figure 16(a). However, in the case of Ni electrodeposition in the presence of a magnetic field, the overpotential changes from the initial value of –760 mV to –500 mV, a much larger decrease of 260 mV during the same period of 1hour deposition time (Fig. 16(b)). This decrease can be due to two reasons. The deposition process increases the microroughness, which can bring down the current density expressed for the true surface area of the nickel

electrode. This, of course, is true for the deposition in the absence of the magnetic field also.

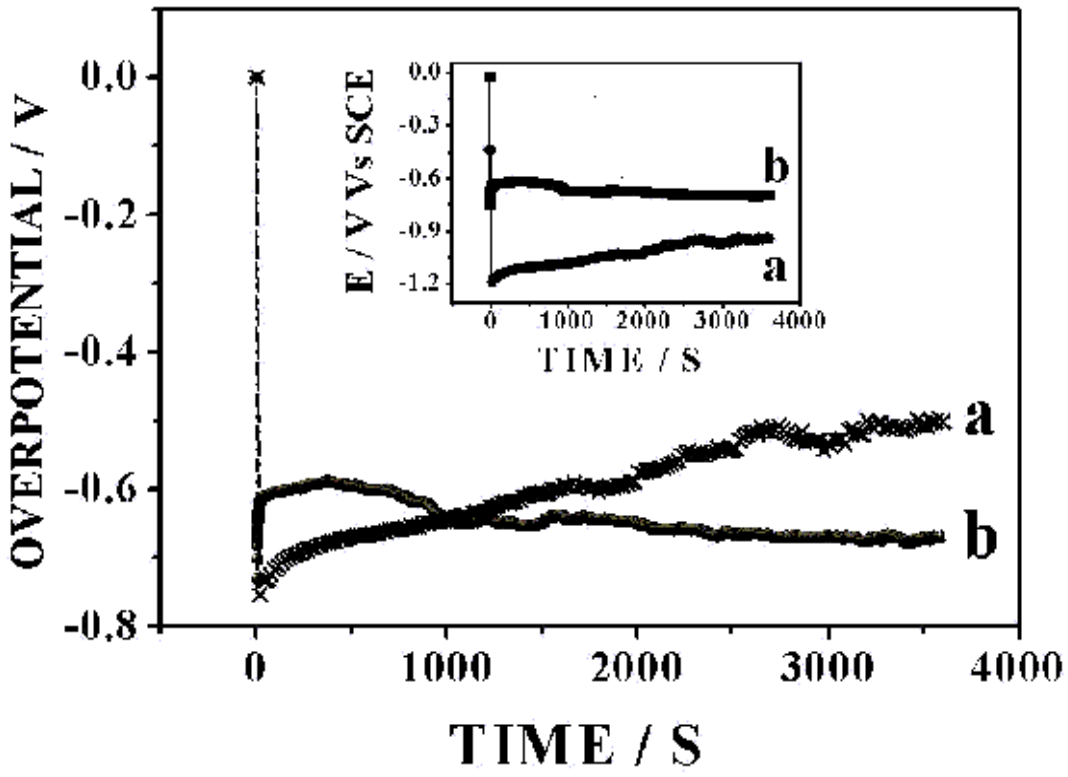

Figure 16: Variation of overpotential with time for the electrodeposition of nickel: (a) in the absence of a magnetic field and (b) in the presence of magnetic field of 1Tesla at an angle of 45^0. Inset shows the initial change of electrode potential on applying magnetic field and its variation as a function of time for the electrodeposited nickel in (a) without magnetic field and (b) with magnetic field.

However, the larger decrease of overpotential in the presence of the magnetic field can be brought about by the large lowering of the concentration gradient due to the convective effect caused by the Lorentz forces. This in turn lowers the concentration overpotential as the deposition proceeds, leading to an

increase of deposition rate. Similar conclusion was arrived for the copper deposition in presence of a constant homogeneous magnetic field by Noninski et al. [69]. The effect of convection induced by the magnetic field has been recently studied by Bund et al. [56]. They find that under the influence of a magnetic field applied parallel to the surface, the limiting current for metal deposition is increased due to the magnetic field induced convection in the Nernst layer. There has been an enhancement in the mass transport of the electroactive species towards the electrode. Using current transients involving deposition and stripping of nickel they show that this process results in a fine-grained deposit with lower crystal size than in the absence of the B field. The crystal size decreases due to increased rate of deposition as this helps in the formation of fresh nucleation centers. In our experiments, we find direct evidence for this process as confirmed by our SEM, STM, XRD and chronopotentiometric studies. The deposition current density of 10 mA/cm^2, which is used in this work is in mixed control at normal average deposition temperature of 50^0C [21] and becomes closer to the limiting current density in the sulphamate bath at lower temperature of 25^0C when there is no external agitation of the electrolyte to increase the mass transport. At this current density in the absence of magnetic field, the deposit produced has a high level of microroughness (Fig. 13(a)). However, in the presence of the magnetic field the deposit is fine grained with several clustered domains and grain boundary regions.

3.6.3.2. Cyclic voltammetry

We have electrochemically characterized the surface roughness of the electrodeposited nickel by cyclic voltammetry in 0.5M NaOH aqueous solution. The roughness factors of the nickel deposits have been determined by

measuring the anodic charge associated with the formation of nickel hydroxide during the cyclic voltammetric measurements in 0.5M NaOH aqueous solution. Figures 17(a) and (b) show the cyclic voltammograms of the nickel surface obtained by carrying out the electrodeposition at 10 mA/cm^2 current density in the absence and in the presence of a magnetic field of 1Tesla respectively. The potential scanning was performed in the potential region where a monolayer of α-$Ni(OH)_2$ is formed at anodic scan and stripped off during the reverse scan beyond -1.0V vs. SCE as seen from the oxide stripping peak [15,70]. The reverse peak of oxide stripping is not seen separately in the diagram as it merges with the hydrogen evolution current. The charge associated with the formation of a monolayer of α-$Ni(OH)_2$ is known to be 514 $\mu C/cm^2$ [15,70] and an estimation of area under the anodic oxidation peak gives an electroactive true surface area from which the roughness factor was calculated. The roughness factor value for nickel in the absence of a magnetic field is 32, which does not differ much from the roughness factor value of 29 obtained in the presence of a magnetic filed. This shows that while the characteristics of the electrodeposited nickel surface change with the magnetic field as evidenced by the growth of nanoparticles and domains of nanoparticles, there is no significant increase in the roughness factor value of the deposit. This again shows that there is no direct correlation between the surface morphology as determined from the electrochemical roughness factor value and grain size. Such a conclusion has been reported by Bund et al. [56] for nickel electrodeposited from Watts nickel bath in the presence of a magnetic field. While these workers have carried out the electrodeposition in the presence of a perpendicular magnetic field, we have applied the magnetic field at an angle of 45^0 orientation. This means that the orientation of the magnetic field does not have any significant effect on the grain morphology a conclusion, which is in

conformity with that of Bund et al. This also implies that the rate of metal deposition is independent of the field orientation, which is similar to the observation of Hinds et al. for copper magnetoelectrolysis [48].

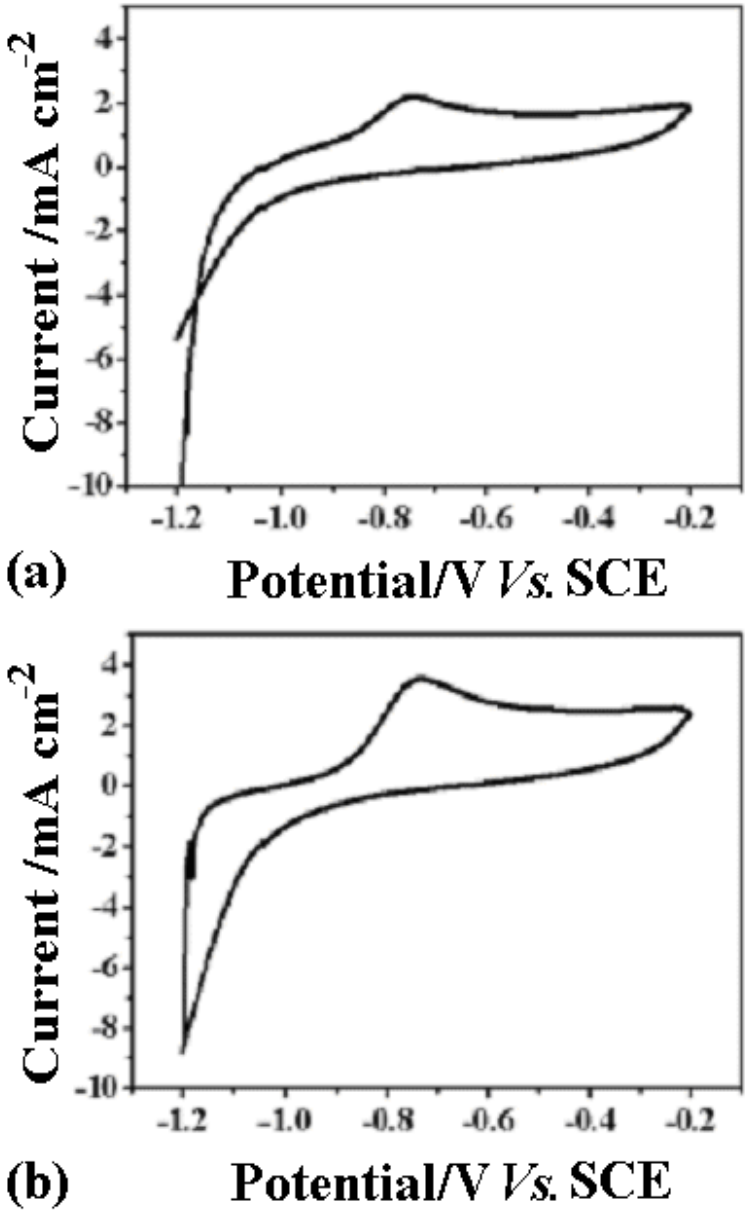

Figure 17: Cyclic voltammograms recorded at a potential scan rate of 50 mV/s in 0.5M NaOH aqueous solution for the nickel deposits obtained at 10 mA/cm^2 current density for about 1hour deposition time for, (a) in the absence of magnetic field and (b) in the presence of a magnetic field of 1Tesla.

3.6.3.3. Current-potential characteristics

Figures 18(a) and (b) show the current–potential plots for the hydrogen evolution reaction on the electrodeposited nickel electrodes in 0.5M NaOH aqueous solution. The slopes of both the plots are around 120 mV/dec, which suggests that the rate-determining step follows Volmer–Heyrovski mechanism [39-42]. There is a significant increase in hydrogen evolution current density by a factor of 3 on the nickel electrode obtained by electrodeposition in the presence of the magnetic field (Fig. 18(b)). This increase of hydrogen evolution current cannot be explained by the rather small decrease of surface roughness factor alone. It is speculated that the nanocrystallites of nickel on the surface may increase the catalytic activity of the electrode as suggested in the literature [71,72]. This aspect, however, has not been studied further in this work, as it needs a separate and more detailed investigation based on the nanoparticles of different size distribution.

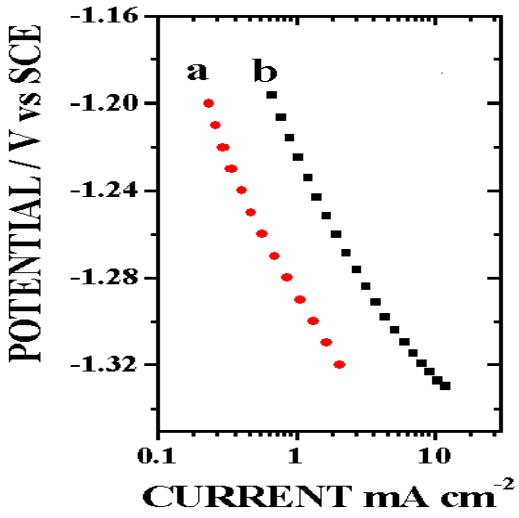

Figure 18: Logarithmic current density vs. potential plots for the electrodeposited nickel: (a) in the absence of magnetic field and (b) in the presence of a magnetic field of 1Tesla applied at an angle of 45^0 to the cathode surface.

3.6.3.4. Electrochemical impedance spectroscopic studies

We have carried out the electrochemical impedance spectroscopic studies at a potential region between -1.2V and -1.4V vs. SCE for the nickel electrodes obtained both in the absence and in the presence of magnetic field in 0.5M NaOH aqueous solution. These studies provide information on the effective surface area available for the hydrogen evolution reaction. The Nyquist plots of the nickel electrode prepared in the presence of a magnetic field of 1Tesla for about 1hour deposition time at different potential values are shown in the figure 19. We find that the nickel electrode exhibits a single semicircle, which can be fitted to the standard Randle's equivalent circuit comprising of a parallel combination of the charge transfer resistance (R_{ct}) and a double layer capacitance (C_{dl}) with a series solution resistance (R_u). The impedance plots of nickel electrodes obtained both in the presence and absence of magnetic field (Figures not shown) does not show any difference in the plots except in their R_{ct} values. The semicircle is potential dependent and the diameter of this semicircle decreases with the overpotential. In addition to this, we observe at high overpotentials a low frequency positive phase angle region corresponding to an inductive element. The low frequency inductive loop for the hydrogen evolution reaction has been earlier proposed by Conway et al. [25] and later experimentally observed by other workers for Ni-Zn [37] and Ni–P [38] alloys in alkaline media. These workers also found a significant absorption of hydrogen and the formation of surface hydride layers in these systems. The reason for the observed inductive behaviour, as can be seen from the figure 19, may be due to the hydride formation at these overpotentials, a conclusion that needs to be confirmed by further investigation. From these experiments, it can be concluded that the applied magnetic field has an effect in the surface

morphology of the deposit by affecting the mass transfer process involved in the electrolysis of nickel.

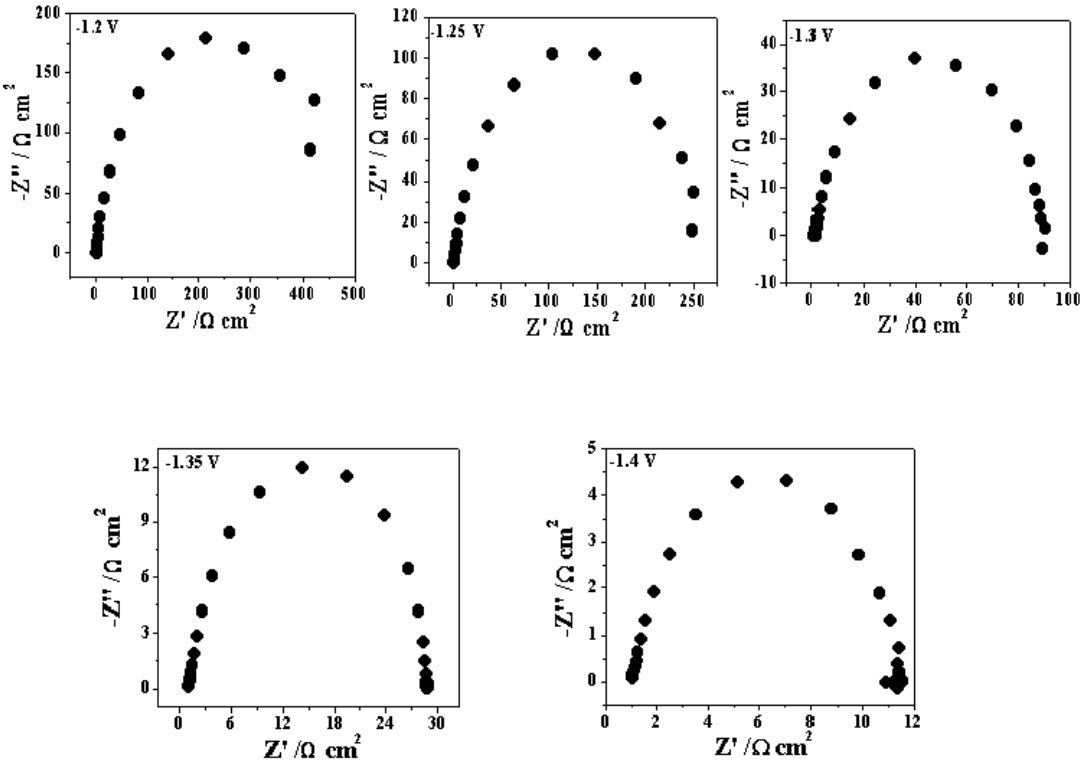

Figure 19: Nyquist plots of deposited nickel electrode in the presence of a magnetic field of 1Tesla in 0.5M NaOH aqueous solution at various potentials in the hydrogen evolution region. Frequency range = 0.1 Hz to 100 kHz.

III. MICROEMULSION PHASE AS A TEMPLATE

3.7. Introduction

Microemulsions are unique class of optically clear, thermodynamically stable and homogeneous solution having low viscosity [73]. These systems were first identified by Hoar and Schulman in 1943 as a special colloidal dispersion and the term 'Microemulsion' was coined in 1958. Microemulsion systems are very useful in the synthesis of nanoparticles of size ranging from 1nm to 100nm where it acts as an inert medium to prevent the coalescence of nanoparticles [74-76]. Using microemulsion, it is possible to entrap the desired nanoparticles in a nanocavity produced by them. The microemulsions are also used to obtain the biocompatible and biodegradable materials, which are often useful in drug delivery. In general, an emulsion is a heterogeneous system, composed of droplets of oil in water (O/W) or the droplets of water dispersed in oil (W/O) [77]. They are not thermodynamically stable and it can be stabilized by suitable surfactants. Microemulsions can be prepared by controlled addition of surfactant to emulsion phase to produce transparent solutions. The main function of surfactant is to reduce interfacial tension by increasing the interfacial pressure. This causes the liberation of surface free energy, which is required for the spontaneous formation of microemulsion and for its thermodynamic stability. The microemulsions are divided into four Winsor types namely, Winsor I, Winsor II, Winsor III and Winsor IV systems based on the Winsor classification of a triphase system [78, 79] containing oil, water and surfactant compositions that has been explained in chapter 1. All of these systems maintain a certain microenvironment, which is used to produce the particles of desired shape and size during template electrodeposition. The size and shape of this cavity depends on the nature of the surfactant and the compositions of the other components. The very basic properties that

differentiate microemulsions from the other colloidal dispersions are light scattering, rheology studies, electrical conductivity, sedimentation and birefringence. There are a variety of techniques such as the determination of particle dimension and shape, diffusion coefficient, aggregation number, viscosity measurements, neutron and low angle X-ray scattering studies, TEM, dielectric relaxation and time resolved fluorescence quenching techniques are used to characterize the microemulsion system.

In our study, we have used a microemulsion phase formed by the ternary mixture of water, Triton X-100 and toluene compositions as a template for the electrodeposition of nickel. The surface morphology of the deposit was characterized by SEM and the electroactive true surface area was determined using the cyclic voltammetric studies.

3.8. Experimental section

3.8.1. Chemicals

Triton X-100 (Spectrochem), toluene (Spectrochem), sodium hydroxide pellets (EMerck), nickel (II) chloride (EMerck), nickel sulphamate (Grauer and Wheel) and boric acid (Sarabhai chemicals) were used in this study. All the chemical reagents used were AnalaR (AR) grade. Millipore water having a resistivity of 18 MΩ cm was used in all the experiments that have been performed at room temperature.

3.8.2. Preparation of a microemulsion phase

A microemulsion phase was prepared from a ternary mixture of Triton X-100, toluene and water. The mixture exists in the microemulsion phase at the room temperature of 25^0C and increasing the concentration of toluene results in the phase transition. The mixture was stirred in a magnetic stirrer at the room

temperature for about half-an-hour and was allowed to attain the equilibrium state of the homogeneous phase and then immediately used for the experimental analysis. All the electrodeposition experiments carried out using this microemulsion phase as a template have been performed at the room temperature of 25^0C. We have also changed the volume-by-volume ratio of Triton X-100 in toluene to water and carried out the electrodeposition experiments in order to analyze the surface roughness of the deposits prepared using this phase as a template.

3.8.3. Nickel electrodeposition through the microemulsion phase

For nickel electrodeposition, we have replaced the aqueous phase of the above-mentioned microemulsion phase using the standard nickel sulphamate bath [21] having the composition: 300 g/l nickel sulphamate, 6 g/l nickel chloride and 30 g/l boric acid. The ternary system of Triton X-100, water and toluene containing the nickel salt solution in place of the aqueous phase showed no phase separation at room temperature implying the homogeneity of the phase of the electroplating bath.

The typical size of a nickel strip used as the substrate for electroplating experiments is 1mm x 5mm x 5mm. These nickel substrates were cut from a 1mm thick Ni foil, which was prepared using the process of electroforming in nickel sulphamate bath of the same composition that has been used for the template electrodeposition of nickel. Before each experiment, the nickel substrate was polished successively in 1000, 1500 grade emery papers followed by polishing in 1μm, 0.3μm and finally in 0.05μm size alumina powder. Before electroplating, the nickel substrates were activated by immersion into a 1:1 HCl in water for a few seconds. A sulphurised nickel bar was used as an anode. The electroplating was carried out at different current densities of 2, 5, 7.5, and 10

mA/cm^2 at 25^0C for about 1-2 hours. The electrodeposited specimen were washed thoroughly with distilled water and then rinsed with millipore water and then immediately used for the analysis and its characterization. The potential during the process of electrodeposition was monitored using chronopotentiometry.

3.8.4. Characterization of nickel deposited electrodes

We have characterized the nickel deposits obtained from the microemulsion phase that has been served as a template using scanning electron microscopy (SEM) and cyclic voltammetry. SEM characterization of the template deposited nickel materials has been done using JEOL JSM-840 A model instrument and the measurement parameters have been shown in the respective diagrams. The electrochemical characterization of the deposit was carried out in an all glass three-electrode electrochemical cell. A platinum foil of large surface area was used as a counter electrode and a saturated calomel electrode (SCE) as a reference electrode but kept in a separate compartment. Cyclic voltammetry was performed in the potential range of –1.2V to –0.2V vs. SCE in 0.5M NaOH aqueous solution at a potential scan rate of 50mV/s. Before the beginning of the experiments, the electrode was maintained at a potential of –1.6V vs. SCE for 600s in 0.5M NaOH aqueous solution. This process reduces the surface oxides present in the deposited material and cathodically cleans the surface by the evolution of hydrogen gas. This is followed by keeping the electrode at a potential of –1.02V vs. SCE in order to oxidize any metal hydrides that are present on the surface. The potential is then scanned from –1.2V to –0.2V vs. SCE to obtain the nickel oxidation and reduction characteristics from which the electroactive surface area has been determined [15]. The cyclic voltammetric studies were performed using an EG&G

potentiostat (model 263A) interfaced to a personal computer (PC) through a GPIB card (National Instruments).

3.9. Results and discussion

3.9.1. Characterization of nickel deposit using SEM

The surface morphology of the nickel deposit obtained by template electrodeposition using the microemulsion phase as a template has been characterized using scanning electron microscopy (SEM). Figure 20 shows the SEM images of the nickel surfaces prepared by template electrodeposition using the microemulsion phase.

Figure 20(a) shows the SEM image of the nickel surface electrodeposited at 5 mA/cm^2 current density for about 60 minutes using the microemulsion phase as a template. A well adherent deposit having a uniform distribution of particles over the surface has been obtained. These particles have an average diameter of typically 1-2μm in size and appear to extend to the full thickness of the coating. The clusters of granular nickel particles can be seen from the figure and it is found to be distributed more or less uniform in their size. There is no porous structure observed in this case of electrodeposition.

Figures 20(b) and (c) show the higher magnification images of the nickel deposit showing the presence of fractal growth of nickel by the agglomeration of nickel particles. Typical size of these particles varies from 1μm to 2μm. A closer examination of these images suggests that these particles are actually made up of still smaller nanoparticles that agglomerate with each other to form the clusters. Although there is no porous structure observed in the nickel deposits, there exists a gap or crack where there is no deposition. This is due to the structure of the microemulsion phase, which consists of a homogeneous phase having water and oil distributed in a uniform manner.

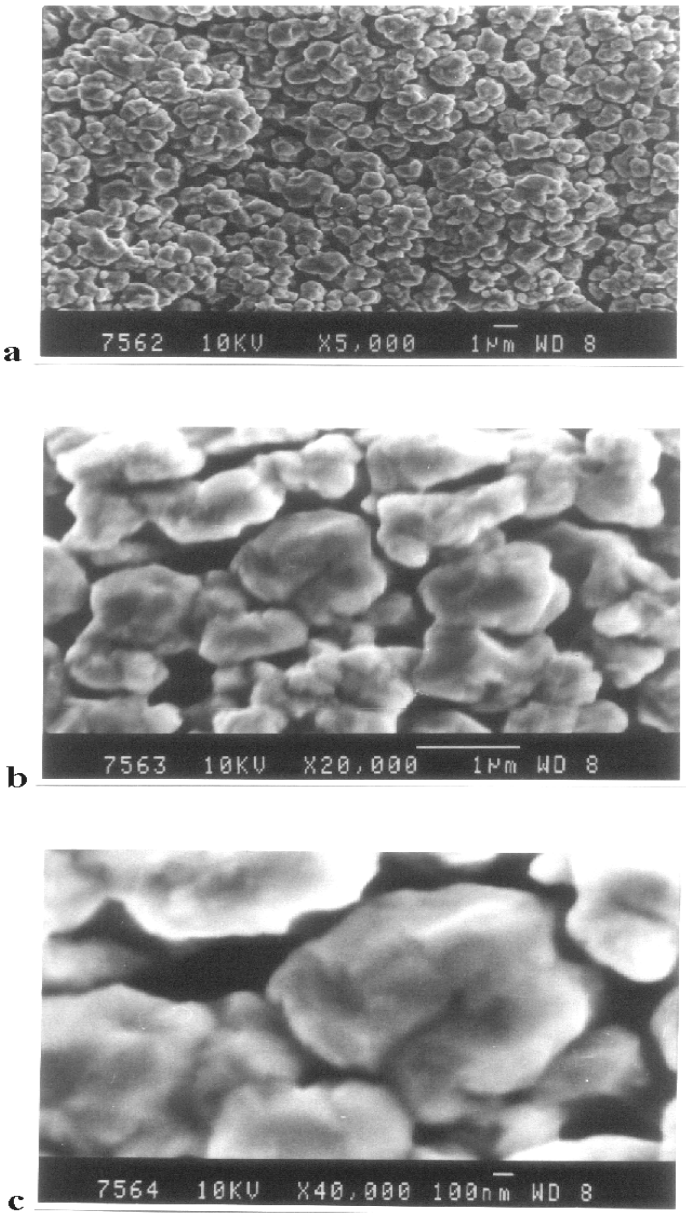

Figure 20: SEM micrographs of nickel electrodeposits prepared at 5 mA/cm^2 current density using: (a) the microemulsion phase consisting of water, Triton X-100 and toluene compositions as a template. (b) and (c) Same as (a) but with higher magnification at a different region showing formation of micron size nickel particles. The other parameters are shown in the respective diagrams.

The electrodeposition occurs only in the aqueous phase and not in the oil phase where it results in the formation of pores. The micron size nickel particles are formed from the aqueous micro domains present in the template. We have also observed no phase separation in the microemulsion phase on applying the electric field during the process of electrodeposition implying the stability and homogeneity of the phase throughout.

3.9.2. Determination of electroactive surface area of the nickel deposit using cyclic voltammetry

The electroactive surface area (true area) of the nickel deposit has been determined by measuring the anodic charge associated with the formation of nickel hydroxide during the cyclic voltammetric measurement in 0.5M NaOH aqueous solution. Figure 21 shows the representative cyclic voltammogram of the nickel electrode obtained by microemulsion template deposition when it is scanned in the potential region where a monolayer of α-$Ni(OH)_2$ is formed during the anodic scan. This monolayer is stripped off during the reverse scan beyond a potential of –1V vs. SCE as can be seen from the oxide-stripping peak [15,36]. However, the CV of the nickel deposit shows a very small oxide formation region in this case unlike that of the porous nickel electrode prepared using the hexagonal liquid crystalline phase as a template. The reverse peak of oxide stripping is not seen separately as it merges with the hydrogen evolution current. The charge associated with the formation of a monolayer of α-$Ni(OH)_2$ is known to be 514 $\mu C/cm^2$ [15,36] and an estimation of the area under the anodic peak gives the measurement of the electroactive true surface area that corresponds to a roughness factor value of 350 in comparison to the roughness factor of 4 obtained for the smooth nickel sample. We have also carried out the

electrodeposition of nickel by changing the volume-by-volume ratio of Triton X-100 in toluene to water and measured the roughness factor values of the deposits using cyclic voltammetry and the corresponding values are given in table 4. It can be seen from the table that the roughness factor value is relatively high for 1:40 v/v ratio, indicating the increase in surface area of the nickel deposit due to the presence of microemulsion phase.

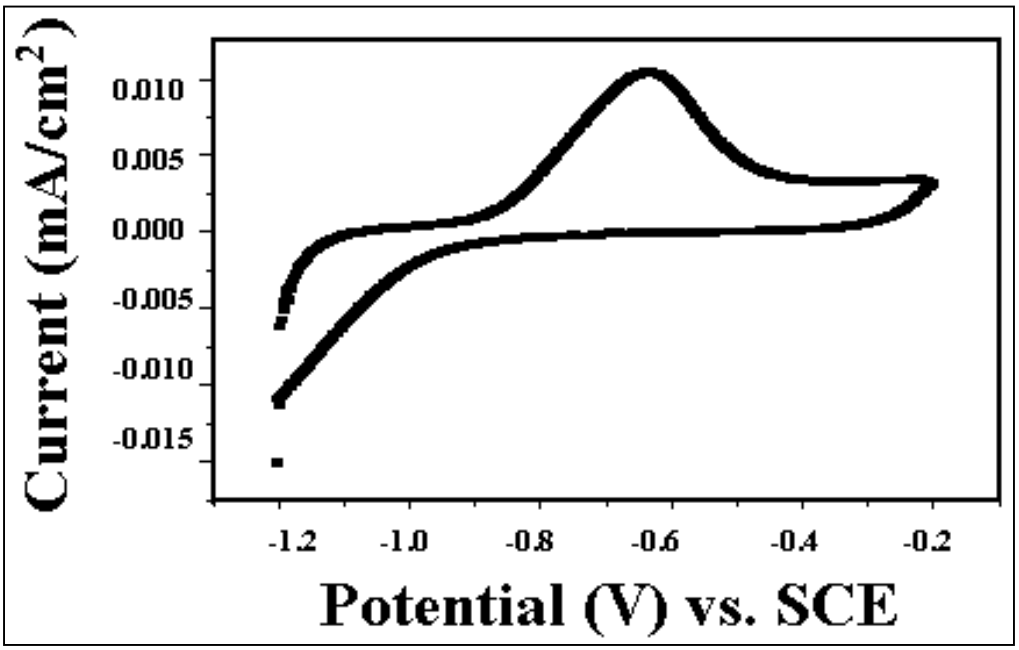

Figure 21: Representative cyclic voltammogram performed at 50mV/s sweep rate recorded in a 0.5M NaOH aqueous solution for the nickel deposit produced by electroplating at 5 mA/cm^2 current density using the microemulsion phase consisting of water - Triton X-100 - toluene composition as a template.

From these experimental studies we find that the template electrodeposition is a very useful technique to produce particles of different size and shape with increased catalytic activity. The surface morphology of the

electrodeposited materials is mainly affected by the mass transfer process in this kind of template electrodeposition.

Table-4

The roughness factor values of different v/v ratios of water-Triton X-100-toluene system determined from the cyclic voltammetric studies.

V/V ratios	Roughness factor (RF) values
1:10	280
1:20	300
1:30	320
1:40	350
1:50	220
1:75	290

IV. ELECTRON TRANSFER STUDIES USING SOME SURFACTANTS SELF-AGGREGATED SYSTEMS AS ELECTROLYTIC MEDIA

3.10. Introduction

In this section, we have described our studies on electron transfer reactions of redox probe molecules using some self-aggregated systems of surfactants as electrolytic media. We have used $[Fe(CN)_6]^{3-|4-}$ and $[Ru(NH_3)_6]^{2+|3+}$ redox couples as probe to study the electron transfer reactions. We have used four different phases viz., (a) micelles formed from sodium dodecyl sulphate (SDS), (b) a microemulsion phase consisting of a ternary mixture of water, Triton X-100 and p-Xylene/toluene, (c) a hexagonal liquid crystalline phase and (d) a lamellar phase consisting of water, Triton X-100 and

decanol compositions as electrolytic media for our investigation. Electrochemical techniques such as cyclic voltammetry and electrochemical impedance spectroscopy were extensively used in our study.

We find from literature that there are some reports on the study of electron transfer reactions in self-aggregated systems of surfactant, especially in the microemulsion phase [80-88]. Sjoblom et al. [80] have reported an excellent review article on microemulsion based on its characterization, structure and applications in chemical reactions. Kamau et al. [81] studied the reduction reactions of some organic compounds in bicontinuous microemulsion phase formed from a ternary mixture of didodecylammonium bromide (DDAB), water and dodecane compositions using nickel and copper phthalocyanine tetrasulphonates mediators. These authors found that the rate of the electron transfer reaction is enhanced in the microemulsion phase due to the enhancement in the catalytic efficiency arises from a different mechanism of electron transfer reaction observed in this phase. Rusling et al. investigated the electron transfer reactions of water-soluble ferrocyanide and ruthenium(III)hexamine and oil soluble ferrocene, pyrene, perylene and 9-phenylanthracene in bicontinuous microemulsion phase of DDAB/water/dodecane system [82,83]. These authors observed a voltammetric behaviour similar to that in homogeneous solution and found that the diffusion coefficients of ferrocyanide and ruthenium(III)hexamine complexes in microemulsion were 5-7 times smaller than in water and for ferrocene it was about one-fourth of its value in acetonitrile [82]. It seemed that the ions dissolved in the aqueous phase diffuse with same diffusion coefficients characteristic of that phase, while the molecules dissolved in the oil phase have the same characteristic diffusion coefficients as the oil phase. Georges and Chen studied the microemulsion structure formed by SDS with pentanol and

heptanol using a variety of techniques such as viscosity, electrical conductivity, electrochemical and fluorescent probe measurements and found a good correlation between the information provided by these techniques and proposed water continuous, bicontinuous and oil continuous structures for the microemulsion phase [84].

Chen et al. [85] reported the electrode reaction of ferrocene in a nitrobenzene/water emulsion containing SDS molecules and found that the ferrocene redox reaction is irreversible in the emulsion phase, which is in contrast to the reversible behaviour observed in organic solvents. These authors also proposed two different mechanisms for the electrode reaction based on the concept of interfacial energy and dispersion of redox probe in the emulsion phase. Hotta et al. proposed a new strategy for characterizing the electron transfer processes at the oil/water interface using electron-conductor separating oil-water (ECSOW) system [86] and showed that this system can be a promising source to clarify many complicated charge transfer processes occurring in biological compounds such as L-ascorbic acid. Minero and Pramauro studied some electron transfer reactions in organic compounds using the microemulsion phase formed by SDS/1-butanol/toluene/water system [87]. Gounili et al. reported the electrochemical diffusion and kinetics studies of some organic reactions in microemulsion phase and ionic micellar medium formed by CTAB and SDS in water [88]. Asami reported the dielectric relaxation studies in water/toluene/ Triton X-100 microemulsion near phase inversion [89] and interpreted the results in terms of interfacial polarization with a percolation model in which the spherical water droplets are arranged in an array in a continuous oil phase and randomly connected with the nearest neighbors using water bonds.

In our work, we have studied the electron transfer reactions of water soluble hexaammineruthenium(III) chloride complex in the micellar medium formed by SDS in water and potassium ferrocyanide complex in the microemulsion, hexagonal liquid crystalline and lamellar phases formed from the ternary system mentioned above. We have used electrochemical techniques such as cyclic voltammetry and electrochemical impedance spectroscopy in our investigation. We have carried out the experiments using macroelectrodes and disk/wire electrodes of gold and platinum.

3.11. Experimental section

3.11.1. Chemicals

Sodium dodecyl sulphate (Acros Organics), Triton X-100 (Spectrochem), toluene (Spectrochem), p-Xylene (Emerck), poly(acrylic acid) (PAA) (Aldrich), decanol (Emerck), potassium ferrocyanide (Loba), potassium ferricyanide (Qualigens), hexaammineruthenium(III) chloride (Alfa Aesar), sodium fluoride (Qualigens) and lithium perchlorate (Acros Organics) were used in this study as received. All the chemical reagents used in our study are AnalaR (AR) grade reagents. Millipore water having a resistivity of 18 MΩ cm was used in all the experiments that have been performed at room temperature.

3.11.2. Preparation of self-aggregated surfactants systems

We have used several self-aggregated surfactants systems namely micelles, microemulsion phase, hexagonal liquid crystalline phase and lamellar phase as electrolytic media for the electron transfer studies of redox couples. The micellar medium was prepared using sodium dodecyl sulphate (SDS) in water and for the electron transfer studies, the redox probe namely, 1mM hexaammineruthenium(III) chloride in 0.1M lithium perchlorate was added to

the aqueous phase. We have carried out the cyclic voltammetry and impedance spectroscopic studies of electron transfer reaction in this micellar medium by increasing the concentration of SDS by 0.5mM at each addition.

The microemulsion phase was prepared from a ternary mixture of Triton X-100, toluene/p-Xylene and water system. The mixture exists in the microemulsion phase at the room temperature of 25^0C and increasing the concentration of toluene results in the phase transition to isotropic phase. The mixture was stirred in a magnetic stirrer at the room temperature for about half-an-hour and was allowed to attain the equilibrium state of the homogeneous phase and then immediately used for the experimental analysis. For the study of electron transfer reaction in this microemulsion phase, the redox couple namely, 10mM potassium ferro/ferri cyanide in 1M NaF was added to the aqueous phase. We have performed cyclic voltammetry and electrochemical impedance spectroscopy to study the redox reaction in this microemulsion phase.

The hexagonal liquid crystalline phase was prepared from a ternary mixture of Triton X-100, decanol and water. The mixture exists in the hexagonal liquid crystalline phase at the room temperature of 25^0C and increasing the concentration of decanol shifts the phase transition to isotropic phase at a temperature above 30^0C. The mixture was stirred in a magnetic stirrer at a temperature of 33^0C – 35^0C for about 1 hour and was allowed to cool down to room temperature. When viewed under a polarized light microscope, the mixture exhibits the characteristic birefringence of a hexagonal liquid crystalline phase, which is stable up to 30^0C. In order to study the electron transfer reaction, the aqueous phase in the hexagonal liquid crystalline phase was replaced by a solution containing 10mM potassium ferro/ferri cyanide in 1M NaF. Similarly, we have prepared the lamellar phase using the same ternary system and for electron transfer studies, the aqueous phase was replaced by the

above-mentioned potassium ferro/ferri cyanide solution. In all these cases, NaF and $LiClO_4$ were used as the supporting electrolytes. Cyclic voltammetry and electrochemical impedance spectroscopy were used for the analysis.

3.11.3. Fabrication of electrodes and electrochemical cell

We have carried out the electron transfer studies in surfactants self-aggregated systems as electrolytic media using macroelectrode (Platinum foil) and wire/disk electrodes (Au and Pt). Gold and Platinum samples of purity 99.99% were obtained from Arora Mathey, India. The gold and platinum wire electrodes were fabricated by proper sealing of a 99.99% pure metal wire of 0.5mm diameter with soda lime glass having a thermal expansion coefficient close to that of the respective metal. The electrical contact has been provided through a copper wire. This planar disc electrode has a geometric area of 0.002 cm^2.

A conventional three-electrode electrochemical cell was used for the electron transfer studies using electrochemical techniques. A platinum foil of large surface area was used as a counter electrode and a saturated calomel electrode (SCE) was used as a reference electrode while either the Pt foil or disk/wire electrodes were used as the working electrode. The cell was cleaned thoroughly before each experiment and kept in a hot-air oven at 100^0C for at least 1 hour before the start of the experiment.

3.11.4. Electrode pre-treatment procedure

Immediately before use, the disk/wire electrode was polished with emery papers of grade 800 and 1500 respectively, followed by polishing in aqueous slurries of progressively finer alumina of sizes ranging from 1.0μm, 0.3μm to 0.05 μm on a microcloth. After this, the electrode was ultrasonicated

in millipore water to remove alumina particles. Then, in the case of gold, the electrode was cleaned in a "piranha" solution, which is a mixture of 30% H_2O_2 and concentrated H_2SO_4 in 1:3 ratio. (*Caution: Piranha solution is very reactive with organic compounds. Storing in a closed container or exposure to direct contact with eye should be avoided.)* In the case of platinum, the electrode was cleaned in conc. HNO_3 for about a minute. Finally, the polished disk/wire electrode was thoroughly cleaned and rinsed in distilled water, followed by rinsing in millipore water and used for the experimental analysis.

3.11.5. Electron transfer studies using electrochemical techniques

Electrochemical techniques such as cyclic voltammetry and electrochemical impedance spectroscopy were used for the electron transfer studies of redox probe molecules in some surfactants self-aggregated systems as electrolytic media. Two different redox probes namely, potassium ferrocyanide (negative redox probe) and hexaammineruthenium(III) chloride (positive redox probe) were used for the electron transfer studies. Cyclic voltammetry was performed at a potential range of 0V to +0.5V vs. SCE to study the redox reaction of potassium ferro/ferri cyanide complex and at a potential range of –0.45V to 0V vs. SCE in the case of hexaammineruthenium(III) chloride complex by using NaF and $LiClO_4$ as the supporting electrolytes in the respective solution. The impedance measurements were carried out using an alternating current (ac) of a 10mV amplitude signal at a formal potential of the redox couple using a wide frequency range of 100kHz to 0.1Hz, in solution containing always equal concentrations of both the oxidized and reduced forms of the redox couple namely, 10mM potassium ferrocyanide and 10mM potassium ferricyanide in 1M NaF as the supporting electrolyte. The other parameters were shown in the respective diagrams.

3.11.6. Instrumentation

The cyclic voltammetric studies were performed using an EG&G potentiostat (model 263A) interfaced to a personal computer (PC) through a GPIB card (National Instruments). For electrochemical impedance spectroscopic studies the potentiostat is used along with an EG&G 5210 lock-in-amplifier controlled by a PC using the Power Sine software. The impedance measurements were carried out between 0.1 Hz and 100 kHz in all the cases. The ZSimpWin software program (EG&G) was used for the analysis of the impedance data and to determine the charge transfer resistance (R_{ct}) values using the equivalent circuit fitting procedure.

3.12. Results and discussion

3.12.1. Electron transfer studies using the micellar medium

We have studied the electron transfer reaction of ruthenium redox couple in the micellar medium formed by SDS in water. Cyclic voltammetry and electrochemical impedance spectroscopy were used for this study. We have carried out these experiments using the gold disk/wire electrode as a working electrode. Figure 22 shows the comparison of cyclic voltammograms of ruthenium redox reaction for bare Au electrode in the aqueous medium (a) and in the micellar medium (b) using 1mM hexaammineruthenium(III) chloride in 0.1M lithium perchlorate as a supporting electrolyte at a potential scan rate of 50 mV/s. It can be seen from the figure 22 (a) that the bare Au electrode shows a diffusion controlled peak shaped voltammogram for the ruthenium redox reaction in the aqueous medium indicating that the electron transfer process is reversible. In contrast, it exhibits a blocking behaviour for the redox reaction of ruthenium complex in the micellar medium (Fig. 22 (b)) implying that the electron transfer process is under charge transfer control. Figure 23 shows the

impedance plots of bare Au electrode in the aqueous medium (a) and in the micellar medium (b) for the redox reaction of ruthenium complex in 1mM hexaammineruthenium(III) chloride with 0.1M $LiClO_4$ as the supporting electrolyte. It can be seen from the figure 23 (a) that the bare Au electrode shows an impedance plot corresponding to a diffusion controlled process for the ruthenium redox species. On the other hand, in presence of micelles, the bare Au electrode exhibits a depressed semicircle in the impedance plot for the ruthenium redox reaction (Fig. 23 (b)) implying that the electron transfer process is charge transfer controlled corresponding to a blocking behaviour of the redox reaction. It is well known that the diameter of the semicircle obtained in the impedance plot is a measure of charge transfer resistance (R_{ct}), which indicates the extent of blocking of the electron transfer reaction. We have determined a charge transfer resistance (R_{ct}) value of 2400 Ω cm^2 for the ruthenium redox reaction in the micellar medium in comparison to 0.22 Ω cm^2 in the aqueous medium using the equivalent circuit fitting procedure, implying that the micellar medium blocks the redox reaction to a very large extent.

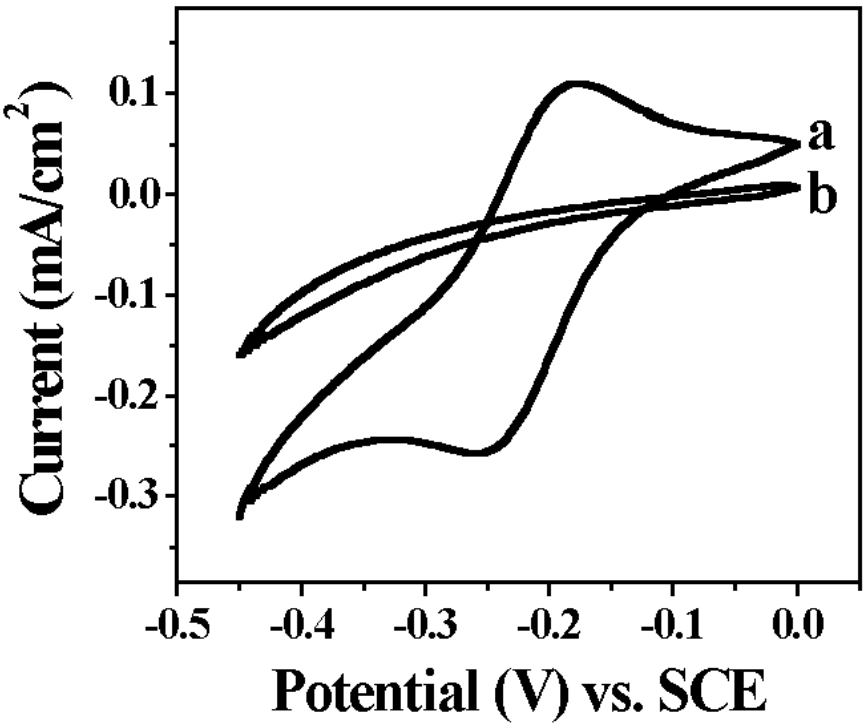

Figure 22: Cyclic voltammograms of bare Au electrode in 1mM hexaammineruthenium(III) chloride with 0.1M $LiClO_4$ as the supporting electrolyte at a potential scan rate of 50 mV/s for, (a) aqueous medium and (b) micellar medium formed from sodium dodecyl sulphate (SDS) in water.

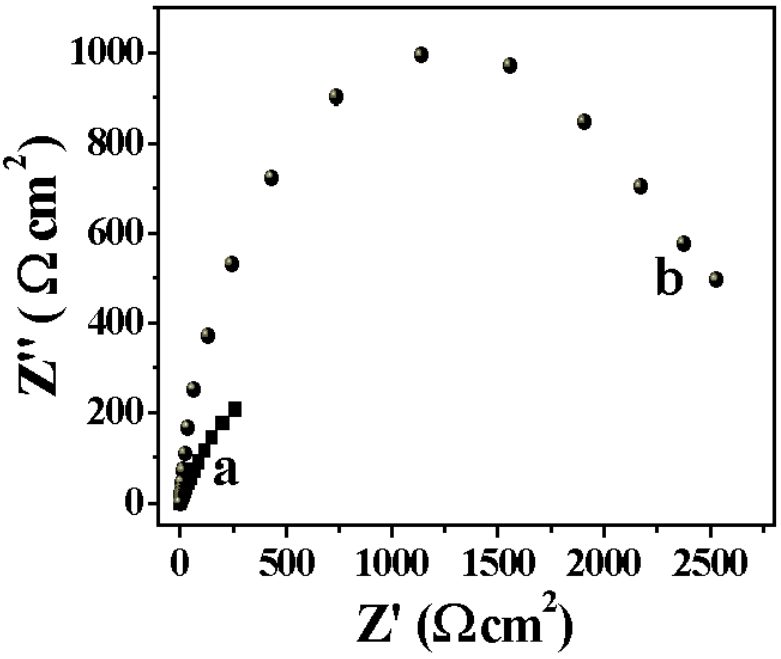

Figure 23: Impedance plots (Nyquist plots) of bare Au electrode in 1mM hexaammineruthenium(III) chloride with 0.1M $LiClO_4$ as the supporting electrolyte for, (a) aqueous medium and (b) micellar medium formed from SDS in water.

We have performed the electron transfer studies of ruthenium redox couple using gold wire electrode in an aqueous solution containing 1mM hexaammineruthenium(III) chloride with 0.1M $LiClO_4$ as the supporting electrolyte by increasing the concentration of SDS by 0.5mM at each addition. This experiment provides information on the electron transfer reaction of ruthenium complex with increasing concentration of SDS. Figure 24 shows the comparison of cyclic voltammograms of ruthenium redox reaction on bare Au electrode in 1mM hexaammineruthenium(III) chloride with 0.1M $LiClO_4$ as the supporting electrolyte at a potential scan rate of 50 mV/s at each addition of

0.5mM SDS. It can be seen from the figure 24 (a) that the bare Au electrode shows a peak shaped voltammogram for the ruthenium redox reaction in the aqueous medium indicating that the electron transfer process is reversible and diffusion controlled. It can also be noted from the CVs that the redox reaction becomes quasi-reversible, irreversible and finally to a blocking behaviour on the addition of SDS implying that the electron transfer process changes from a diffusion controlled process to a charge transfer controlled process with increasing SDS concentration. This implies that the process of diffusion of redox species drastically changes from the aqueous solution to the micellar medium.

Figure 25 shows the impedance plots of bare Au electrode in 1mM hexaammineruthenium(III) chloride with 0.1M $LiClO_4$ as the supporting electrolyte for each addition of 0.5mM SDS. It can be seen from the figure 25 (a) that the bare Au electrode shows a straight line in the entire range of frequency used for the study indicating a diffusion controlled process for the ruthenium electron transfer reaction. It can also be observed from the impedance plots that on increasing the concentration of SDS, the corresponding impedance plots changes from a straight line to a depressed semicircle implying that the electron transfer process changes from a diffusion control to a charge transfer controlled process. The formation of semicircle indicates a blocking behaviour for the redox reaction of ruthenium complex.

It can also be noted from the impedance plots (Fig. 25) that the R_{ct} value increases with the increasing concentration of SDS. From these experiments, it is clear that the diffusion process involved in the electron transfer reaction differs from the aqueous solution to the micellar medium. These results are in conformity with that of the cyclic voltammetric results discussed earlier.

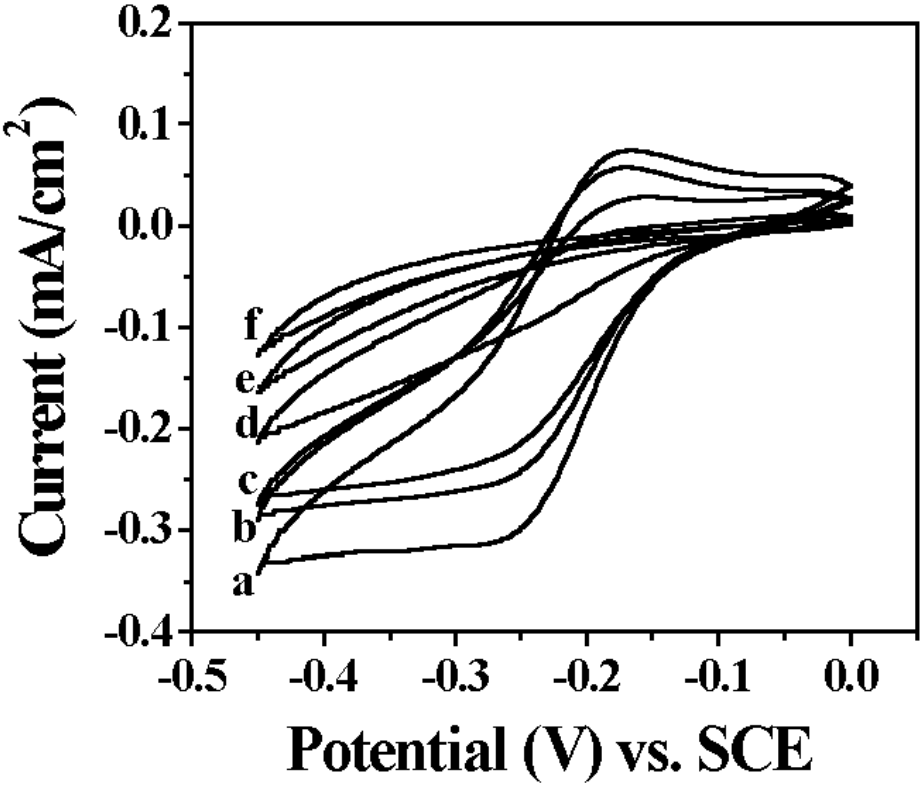

Figure 24: Comparison of cyclic voltammograms of bare Au electrode in 1mM hexaammineruthenium(III) chloride with 0.1M $LiClO_4$ as the supporting electrolyte at a potential scan rate of 50 mV/s for each addition of 0.5mM SDS. (a) 0mM, (b) 0.5mM, (c) 1mM, (d) 1.5mM, (e) 2mM and (f) 3mM concentrations of SDS in water.

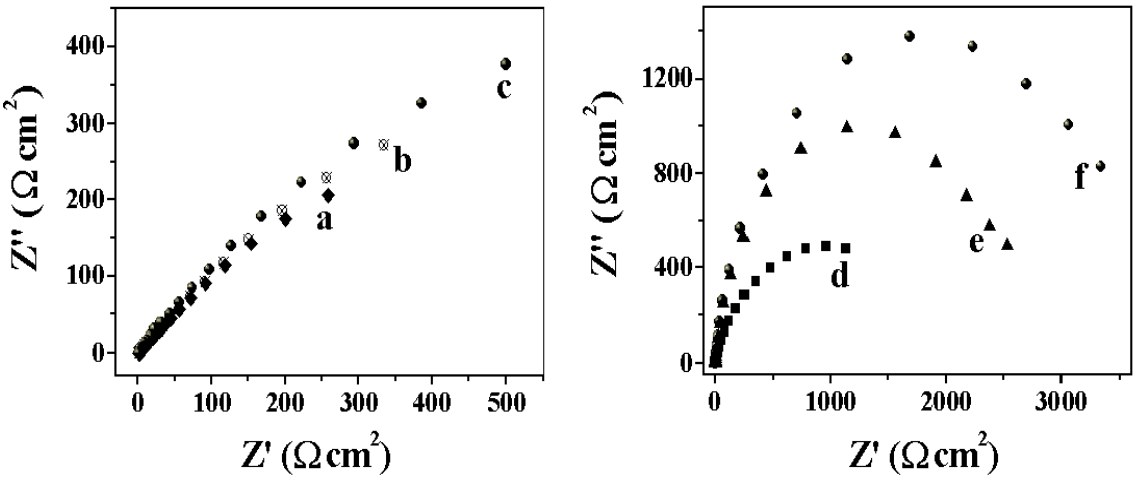

Figure 25: Typical impedance plots of bare Au electrode in 1mM hexaammineruthenium(III) chloride with 0.1M $LiClO_4$ as the supporting electrolyte for each addition of 0.5mM SDS. (a) 0mM, (b) 0.5mM, (c) 1mM, (d) 1.5mM, (e) 2mM and (f) 3mM concentrations of SDS in water.

Based on the cyclic voltammetry and electrochemical impedance spectroscopic studies, we find that the electron transfer reaction of ruthenium complex changes from a diffusion controlled process to a charge transfer controlled process when the electrolytic medium is changed from an aqueous solution to the micellar medium. This is due to the semi-infinite linear diffusion of redox species in the aqueous solution that has been changed to a radial diffusion in the micellar medium. The structure of the micellar medium formed by SDS consists of dispersion of oil in water phase, where the direct access of redox species to the electrode surface is prevented by the oil droplets in the micelles that act as an array of microelectrodes. This changes the process of diffusion of redox species from linear to radial diffusion and slows down the

diffusion process. This has been further confirmed by the large increase in the R_{ct} value of the ruthenium redox reaction in the micellar medium.

3.12.2. Electron transfer studies using the microemulsion phase

In this section, we discuss about the electron transfer studies of potassium ferro/ferri cyanide redox couple in the microemulsion phase formed from a ternary mixture of Triton X-100, water and toluene/p-Xylene compositions. We have used electrochemical techniques such as cyclic voltammetry and electrochemical impedance spectroscopy for the experimental analysis. We have used macroelectrode (Pt foil) and disk/wire electrode as the working electrode in our studies. Figure 26 shows the comparison of cyclic voltammograms of bare platinum foil electrode in the aqueous medium (a) and in the microemulsion phase (b) using 10mM potassium ferrocyanide with 1M NaF as the supporting electrolyte at a potential scan rate of 50 mV/s. It can be seen from the figure that the bare platinum foil electrode exhibits a peak shaped voltammogram for the redox reaction implying that the electron transfer process is under diffusion control and is reversible in the aqueous medium (Fig. 26 (a)). On the other hand, it exhibits a blocking behaviour, which is characteristic of an array of microelectrodes in the microemulsion phase formed by the ternary mixture of water, Triton X-100 and toluene compositions (Fig. 26 (b)) indicating that the redox reaction is charge transfer controlled.

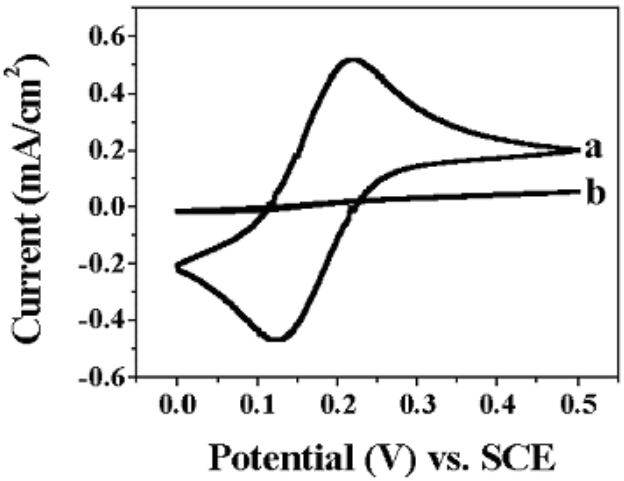

Figure 26: Cyclic voltammograms of bare platinum foil electrode in 10mM potassium ferrocyanide with 1M NaF as the supporting electrolyte at a potential scan rate of 50 mV/s for, (a) aqueous medium and (b) the microemulsion phase formed from a ternary mixture of water, Triton X-100 and toluene compositions.

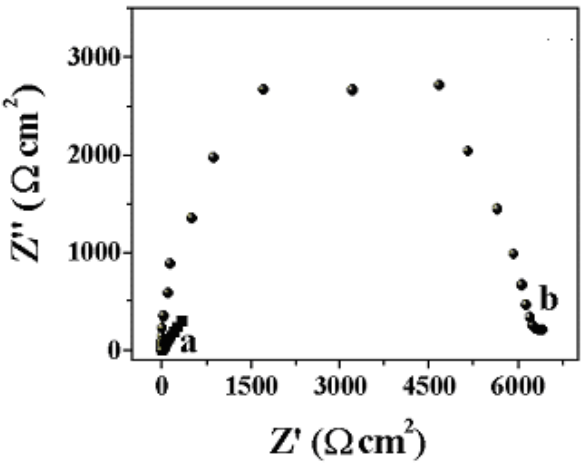

Figure 27: The impedance plots of bare platinum foil electrode in 10mM potassium ferrocyanide and 10mM potassium ferricyanide with 1M NaF as the supporting electrolyte for, (a) aqueous medium and (b) the microemulsion phase formed from a ternary mixture of water, Triton X-100 and toluene compositions.

Figure 27 shows the impedance plots (Nyquist plots) of bare platinum foil electrode in the aqueous medium (a) and in the microemulsion phase (b) for the redox reaction of potassium ferro/ferri cyanide complex in 10mM potassium ferrocyanide and 10mM potassium ferricyanide with 1M NaF as the supporting electrode. It can be seen from the figure that the platinum electrode shows a very small semicircle at higher frequencies and a straight line at lower frequencies in the aqueous medium (a) indicating the electron transfer process is under diffusion control. In contrast, in the case of microemulsion phase, the impedance plot exhibits a semicircle in the entire range of frequency used for the study implying that the electron transfer process is charge transfer controlled and it shows a blocking behaviour characteristic of an array of microelectrodes. Using equivalent circuit fitting procedure, we have determined a charge transfer resistance (R_{ct}) value of 6170 Ω cm^2 for the redox reaction of potassium ferro/ferri cyanide complex in the microemulsion phase in comparison to 1.44 Ω cm^2 in the aqueous medium. This implies that the electron transfer reaction is blocked to a very large extent in the microemulsion phase. These results are in conformity with our CV results discussed earlier.

In order to understand the mechanism of electron transfer process in the microemulsion phase, we have carried out the experiments involving the study of redox reaction of potassium ferrocyanide complex by changing the concentration of toluene using the platinum wire/disk electrode as a working electrode. Figure 28 shows the comparison of cyclic voltammograms of bare platinum electrode in 10mM potassium ferrocyanide with 1M NaF as the supporting electrolyte at a potential scan rate of 50 mV/s by changing the concentration of toluene. It can be seen from the figure that the bare platinum electrode shows a peak shaped voltammogram for the redox reaction in the aqueous medium (Fig. 28 (a)) indicating that the electron transfer process is

under diffusion control and reversible. It can also be noted that on increasing the concentration of toluene the redox reaction changes from a reversible process to quasi-reversible, irreversible and finally to a blocking behaviour characteristic of an array of microelectrodes when the microemulsion phase is formed. This implies that the electron transfer reaction changes from a pure diffusion controlled process to a charge transfer controlled process with increase in toluene concentration until it forms the microemulsion phase. These experiments clearly demonstrate that the process of diffusion of the redox species changes with the change in the electrolytic phase characteristics.

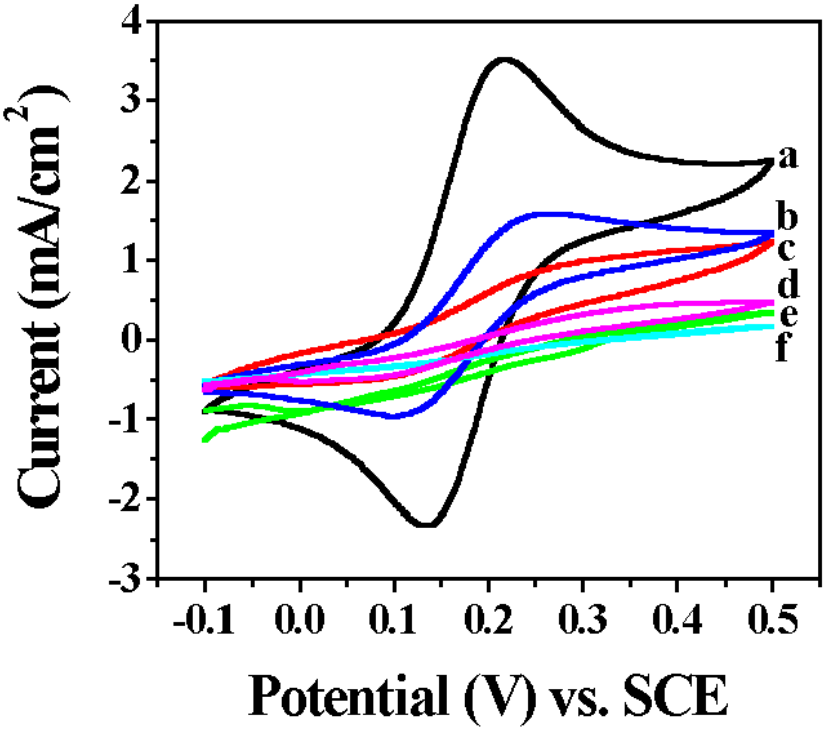

Figure 28: Comparison of cyclic voltammograms of bare platinum electrode in 10mM potassium ferrocyanide with 1M NaF as the supporting electrolyte at a potential scan rate of 50 mV/s for increasing concentration of toluene.

From our experiments involving the study of electron transfer reaction of potassium ferro/ferri cyanide redox couple using cyclic voltammetry and electrochemical impedance spectroscopy, we find that the redox reaction is inhibited and charge transfer controlled in the microemulsion phase in contrast to the aqueous phase where the redox reaction is reversible and diffusion controlled. We believe that the structure of the microemulsion phase formed by the ternary mixture at the interface plays a vital role in the electron transfer process. The blocking behaviour characteristic of an array of microelectrodes exhibited by platinum electrode in the microemulsion phase indicates the radial diffusion process (hemi spherical diffusion) for the redox species in contrast to the semi-infinite linear diffusion observed in the case of aqueous medium. The diffusion of redox species is slower in the microemulsion phase, which slows down the rate of the electron transfer reaction when compared to the rate of the reaction in the aqueous medium. This has been further strengthened by the fact that the R_{ct} value of the redox reaction is significantly higher in the microemulsion phase when compared to the aqueous medium. These experiments clearly show that the electron transfer reaction in the microemulsion phase is under charge transfer control and exhibits a microelectrode array characteristic and it is dominated by the radial diffusion of redox species. Similar results were obtained for the study of electron transfer reaction in the microemulsion phase containing water, Triton X-100 and p-Xylene compositions.

3.12.3. Electron transfer studies using the liquid crystalline phases

We have carried out the electron transfer studies of potassium ferro/ferri cyanide redox couple using the liquid crystalline phases such as the hexagonal liquid crystalline phase and the lamellar phase formed by a ternary

system consisting of water, Triton X-100 and decanol compositions as the electrolytic media. We have used electrochemical techniques such as cyclic voltammetry and electrochemical impedance spectroscopy for our experimental analysis. Figure 29 shows the comparison of cyclic voltammograms of bare Au wire electrode in 10mM potassium ferrocyanide with 1M NaF as the supporting electrolyte at a potential scan rate of 50 mV/s using the aqueous medium (a) and the hexagonal liquid crystalline phase as the electrolytic media. It can be seen from the figure that the electron transfer reaction of potassium ferrocyanide complex exhibits a peak shaped voltammogram in CV indicating that the redox reaction is fully diffusion controlled and reversible in the hexagonal liquid crystalline phase (Fig. 29 (b)), which is similar to the results obtained in the aqueous medium (Fig. 29 (a)). Figure 30 shows the impedance plots of bare Au wire electrode in 10mM potassium ferrocyanide and 10mM potassium ferricyanide with 1M NaF as the supporting electrolyte using the aqueous phase and the hexagonal liquid crystalline phase as the electrolytic media. It can be noted from the figure that the impedance plots show a very small semicircle at higher frequency region and a straight line at lower frequency region for the redox reaction in the hexagonal liquid crystalline phase (Fig. 30 (b)), which is similar to the aqueous medium (Fig. 30 (a)), implying that the electron transfer reaction is under diffusion control and reversible. We have obtained similar results for the lamellar phase formed from the same ternary system that has been used as an electrolytic medium. These experiments clearly show that the electron transfer reaction is fully allowed in the liquid crystalline phases and it does not show any blocking behaviour. The electron transfer reaction in these liquid crystalline phases occurs by the diffusion of redox species through the aqueous medium that is formed by the

interconnection of cylindrical rods resulting in a semi-infinite linear diffusion similar to that of the aqueous medium.

The work carried out during the course of this investigation on the electron transfer studies in some surfactants self-aggregated systems is of preliminary and exploratory nature. A more detailed study is needed to realize the full potentialities of these fascinating systems.

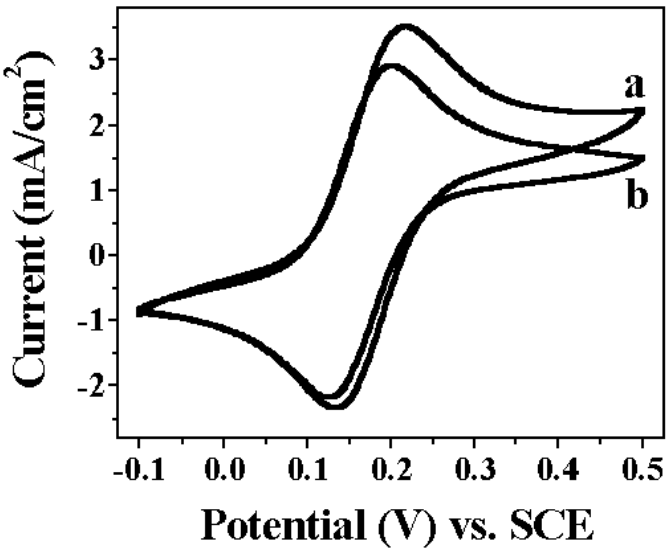

Figure 29: Cyclic voltammograms of bare Au wire electrode in 10mM potassium ferrocyanide with 1M NaF as the supporting electrolyte at a potential scan rate of 50 mV/s for, (a) aqueous medium and (b) the hexagonal liquid crystalline phase obtained from the ternary system.

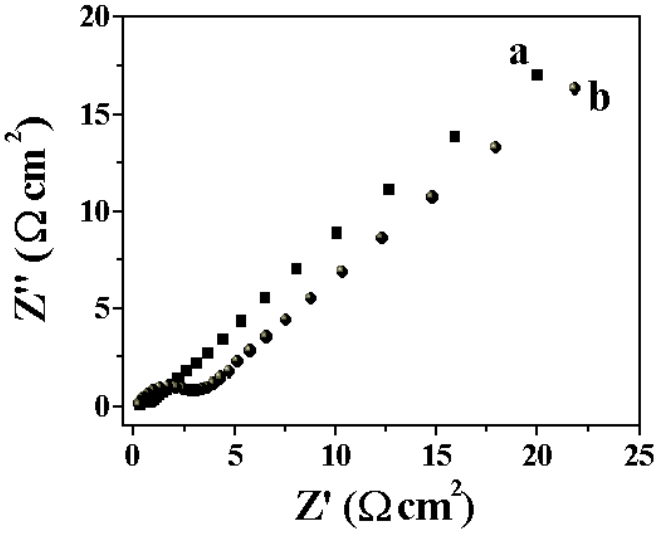

Figure 30: The impedance plots of bare Au wire electrode in 10mM potassium ferrocyanide and 10mM potassium ferricyanide with 1M NaF as the supporting electrolyte for, (a) aqueous medium and (b) the hexagonal liquid crystalline phase obtained from the ternary system.

3.13. Conclusions

In this chapter, we have studied the surface morphology and electrochemical properties of nickel material prepared by the template electrodeposition using a new hexagonal liquid crystalline phase and a microemulsion phase as templates. In addition to this, we have also investigated the effect of applied magnetic field on the electrodeposition of nickel. We have developed a new hexagonal liquid crystalline phase containing the components of nickel electroplating bath, which produces a very high surface area nickel deposit at room temperature. These template-electrodeposited materials show a very high roughness factor value of up to 3620, the highest value reported for nickel in the literature so far other than Raney nickel. The use of liquid

crystalline phase as a template overcomes the problems normally associated with the fabrication and removal of the material after the electrodeposition. Besides, the liquid crystalline phase is obtained from a common available surfactant, Triton X-100. The double layer capacitance value for a single electrode is determined to be 338 mF/cm^2. The capacitance value in the nickel oxide region is measured to be 50 F/g of nickel, suggesting a possible application in the electrochemical capacitors. The very high roughness factor obtained is due to the formation of porous structure and densely distributed nanoscale particles in between as well as inside of the pores. The existence of individual nanoparticle is confirmed by STM images and XRD analysis. The pore formation may be due to the effective screening of the substrate by the liquid crystalline aggregates, which prevents the access of Ni ions from the solution to the electrode surface. The electrochemical characterization using electrochemical impedance spectroscopic studies and current-potential plots for the hydrogen evolution reaction demonstrate the effectiveness of this material to perform as a good electrocatalyst.

We have also studied the effect of externally applied magnetic field on the electrodeposition of nickel using a standard nickel sulphamate bath. Our results suggest that there is an increase in mass transfer rate of Ni ions due to magnetic field induced convection. This increases the rate of deposition leading to the formation of fine-grained deposit. The smallest grains are about 17-25 nm in size as seen by STM and confirmed by XRD. These nanoparticles in turn constitute bigger particles and larger domains. The SEM micrographs of the deposit show that the nanoparticles are spherical in shape, well distributed and mostly concentrated at the domain boundaries. Electrochemical studies using chronopotentiometry show that there is a significant decrease in overpotential with time during the metal deposition process under the applied magnetic field.

This large lowering of the overpotential is due to increase in the rate of metal deposition brought about by the enhanced mass transfer of the Ni ions. There is also a large negative shift in rest potential on the application of a magnetic field of 1Tesla. This is explained on the basis of change in chemical potential of the ferromagnetic metal like nickel that has been brought about by the domain movements and consequent shift in Fermi energy levels due to the application of magnetic field. Our results clearly demonstrate that the magnetic field induced convective mass transfer leads to a fine grain deposit for nickel, in contrast to a layer type growth in the absence of magnetic field.

We have also carried out the template electrodeposition of nickel using the microemulsion phase consisting of water, Triton X-100 and toluene composition as a template. We have characterized the surface morphology of the deposit using SEM. The electroactive true surface area of the nickel deposit has been determined by cyclic voltammetry. We have obtained a fractal growth of nickel surface having the particle size ranging from 1μm to 2μm in diameter. There is no pore formation in this case unlike that of hexagonal liquid crystalline phase template deposition.

We have also performed some preliminary experiments on the electron transfer studies of redox probe molecules using some surfactants self-aggregated systems as electrolytic media. We have used several surfactants aggregate systems such as micelles formed from SDS in water, a microemulsion phase containing the ternary mixture of water, Triton X-100 and toluene/p-Xylene compositions, a hexagonal and a lamellar liquid crystalline phases consisting of a ternary system of water, Triton X-100 and decanol components. We have studied the electron transfer reactions of two different redox couples viz., $[Fe(CN)_6]^{3-|4-}$ and $[Ru(NH_3)_6]^{2+|3+}$ as probe molecules. We find from our cyclic voltammetric and electrochemical impedance

spectroscopic studies that the electron transfer reaction is under charge transfer control and it exhibits the characteristics of microelectrode array behaviour in micelles and in the microemulsion phase that have been used as the electrolytic media. On the other hand, the liquid crystalline phases show a diffusion-controlled process for the electron transfer reactions. We believe that the structure of these surfactants self-aggregated systems at the interface plays a vital role in the mechanism of redox reactions. We also find that the electron transfer reaction is mainly controlled by a radial diffusion (hemi-spherical diffusion) in the cases of micelles and the microemulsion phase, which is in contrast to that of semi-infinite linear diffusion observed in the case of liquid crystalline phases that is similar to that of the aqueous medium. This is further strengthened by the charge transfer resistance (R_{ct}) values determined from the impedance data using the equivalent circuit fitting procedure. Our studies on the electron transfer reaction in these electrolytic media are preliminary and further experiments are needed to understand the mechanism of these redox reactions completely.

References

1. G.S. Attard, P.N. Bartlett, N.R.B. Coleman, J.M. Elliot, J.R. Owen, J.H. Wang, *Science*, 278, (1997), 838.
2. M.H. Lee, S. Geun oh, K.D. Suh, D.G. Kim, D. Sohn, *Colloids surf. A*, 210, (2002), 49.
3. L. Huang, H. Wang, Z. Wang, A. Mitra, K.N. Bozhilov, Y. Yan, *Adv. Mater.*, 14, (2002), 61.
4. Y.X. Pang, X. Bao, *J. Mater. Chem.*, 12[advanced article], (2002), 1-11.
5. S. Sotiropoulos, I.J. Brown, G. Akay, E. Lester, *Mater.Lett.*, 35, (1998), 383.
6. G.S. Attard, C.G. Goltner, J.M. Corker, S. Henke, R.H. Templer, *Angew. Chem. Int. Ed. Engl.*, 36, (1997), 1315.
7. G.S. Attard, J.C. Glyde, C.G. Goltner, *Nature*, 378, (1995), 366.
8. S. Xu, Y. Li, *J. Mater. Chem.*, 12[advanced article], (2002), 1-5.
9. Y. Xiong, Y. Xie, J. Yang, R. Zhang, C. Wu, G. Du, *J. Mater. Chem.*, 12 [advanced article], (2002), 1-8.
10. J. Tanori, M.P. Pileni, *Langmuir*, 13, (1997), 639.
11. A.J. Yin, J. Li, W. Jain, A.J. Bennett, J.M. Xu, *Appl. Phys. Lett.*, 79, (2001), 1039.
12. P.N. Bartlett, T. Dunford, M.A. Ghanem, *J. Mater. Chem.*, 12 [advanced article], (2002), 1-10.
13. R. Simpraga, G. Tremiliosi-Filho, S.Y. Qian, B.E. Conway, *J. Electroanal. chem.*, 424, (1997), 141.
14. S. Rausch, H.Wendt, *J. Electrochem. Soc.*, 143, (1996), 2852.
15. I.J. Brown, S. Sotiropoulos, *Electrochim. Acta*, 46, (2001), 2711.
16. K.W. Nam, K.B. Kim, *J. Electrochem. Soc.*, 149, (2002), A346.

17. V. Srinivasan, J.W. Weidner, *J. Electrochem. Soc.*, 147, (2000), 880.
18. K.W. Nam, W.S. Yoon, K.B. Kim, *Electrochim. Acta*, 47, (2002), 3201.
19. P.A. Nelson, J.R. Owen, *J. Electrochem. Soc.*, 50, (2003), A1313.
20. A.N. Galatanu, I.S. Chronakis, D.F. Anghel, A. Khan, *Langmuir*, 16, (2000), 4922.
21. *Modern Electroplating*, by F.A. Lowenheim, Third edition, John Wiley & sons, New York, (1974), p. 314.
22. (a). V. Lakshminarayanan, *Curr. Sci.*, 74, (1998), 413. (b). M. Jayadeviah, V. Lakshminarayanan, *Meas. Sci. Technol.*, 15, (2004), N32.
23. *The basics of crystallography and diffraction;* by C. Hammond, Oxford University Press: Oxford, (1997).
24. R.D. Tilley, D.A. Jefferson, *J. Mater. Chem.*, 12 [advanced article], (2002), 1-9.
25. D.A. Harrington, B.E. Conway, *Electrochim. Acta*, 32, (1987), 1703.
26. C. Hitz, A. Lasia, *J. Electroanal. chem.*, 500, (2001), 213.
27. R.K. Shervedani, A. Lasia, *J. Electrochem. Soc.*, 145, (1998), 2219.
28. L. Chen, A. Lasia, *J. Electrochem. Soc.*, 139, (1992), 3214.
29. E.B. Castro, M.J. de Giz, E.R. Gonzalez, J.R. Vilche, *Electrochim. Acta*, 42, (1997), 951.
30. R. de Levie, *J. Electroanal. chem.*, 261, (1989), 1.
31. H. Keiser, K.D. Beccu, M.A. Gutjahr, *Electrochim. Acta*, 21, (1976), 539.
32. A. Hasbach, U. Retter, K. Siegler, W. Kautek, *J. Electroanal. chem.*, 561, (2004), 29.
33. V. Lakshminarayanan, R. Srinivasan, D. Chu, S. Gilman, *Surf. sci.*, 392, (1997), 44.
34. K. Beyer, *J. Colloid Interface Sci.*, 86, (1982), 73.
35. *Elements of X-ray diffraction*, by B.D. Cullity, Addison–Wesley, (1956),

p: 262.

36. I.J. Brown, S. Sotiropoulos, *J. Appl. Electrochem.*, 30, (2000), 107.
37. A.C.D. Angelo, A. Lasia, *J. Electrochem. Soc.*, 142, (1995), 3313.
38. I. Paseka, *Electrochim. Acta*, 44, (1999), 4551.
39. S. Trasatti, in *Advances in Electrochemical Science and Engineering*, H. Gerischer and C.W. Tobias (Eds.), VCH, Weinheim, 1992, Vol. 2, p: 38.
40. S.A.S. Machado, L.A. Avaca, *Electrochim. Acta*, 39, (1994), 1385.
41. R. Simpraga, B.E. Conway, *Electrochim. Acta*, 43, (1998), 3045.
42. A. N. Correia, S.A.S. Machado, *Electrochim. Acta*, 43, (1998), 367.
43. T.Z. Fahidy, *Prog. Surf. Sci.*, 68, (2001), 155.
44. T.Z. Fahidy, *J. Appl. Electrochem.*, 13, (1983), 553.
45. R.A. Tacken, L.J.J. Janssen, *J. Appl. Electrochem.*, 25, (1995), 1.
46. A. Chiba, T. Nimi, H. Kitayama, T. Ogawa, *Surf. Coat. Technol.*, 29, (1986), 347.
47. A. Chiba, T. Ogawa, *Chem. Abstr.*, 108, (1988), 175888.
48. G. Hinds, J.M.D. Coey, M.E.G. Lyons, *J. Appl. Phys.*, 83, (1998), 6447.
49. G. Hinds, F.E. Spada, J.M.D. Coey, T.R. Ni Mhiochain, M.E.G. Lyons, *J. Phys. Chem. B*, 105, (2001), 9487.
50. J.M.D. Coey, G. Hinds, *J. Alloys and compounds.*, 326, (2001), 238.
51. T.Z. Fahidy, *Electrochim. Acta*, 35, (1990), 929.
52. R. Aogaki, K. Fueki, *J. Electrochem. Soc.*, 131, (1984), 1295.
53. T.Z. Fahidy, *Chem. Eng. J.*, 17, (1979), 245.
54. O. Lioubashevski, E. Katz, I. Wilner, *J. Phys. Chem. B*, 108, (2004), 5778.
55. M. Waskaas, Y.I. Kharkats, *J. Electroanal. Chem.*, 502, (2001), 51.
56. A. Bund, S. Koehler, H.H. Kuehnlein, W. Plieth, *Electrochim. Acta*, 49, (2003), 147.
57. L. Yang, *J. Electrochem. Soc.*, 101, (1954), 456.

58. M. Perakh, *J. Electrochem. Soc.*, 122, (1975), 1260.
59. A. Chiba, K. Kitamura, T. Ogawa, *Surf. Coat. Technol.*, 27, (1986), 83.
60. J.C. Shannon, Z.H. Gu, T.Z. Fahidy, *J. Electrochem. Soc.*, 144, (1997), L314.
61. J.C. Shannon, Z.H. Gu, T.Z. Fahidy, *J. Appl. Electrochem.*, 29, (1999), 577.
62. E. Brillas, J. Rambla, J. Casado, *J. Appl. Electrochem.*, 29, (1999), 1367.
63. J. Rambla, E. Brillas, J. Casado, *J. Appl. Electrochem.*, 29, (1999), 1211.
64. O. Devos, A. Olivier, J.P. Chopart, G. Maurin, *J. Electrochem. Soc.*, 145, (1998), 401.
65. O. Devos, O. Aaboubi, J.P. Chopart, E. Merienne, A. Olivier, J. Amblard, *J. Electrochem. Soc.*, 145, (1998), 4135.
66. H. Matsushima, T. Nohira, I. Mogi, Y. Ito, *Surf. Coat. Technol.*, 179, (2004), 245.
67. S. Bodea , L. Vignon, R. Ballou, P. Molho, *Phys. Rev. Lett.*, 83, (1999), 2612.
68. H. Shimada, Y. Ootuka, *Phys. Rev. B*, 64, (2001), 235418.
69. V.C. Noninski, *Electrochim. Acta*, 42, (1997), 251.
70. I.J. Brown, S. Sotiropoulos, *J. Appl. Electrochem.*, 30, (2000), 107.
71. C.N.R. Rao, G.U. Kulkarni, P.J. Thomas, P.E. Edwards, *Chem. Eur. J.*, 8, (2002), 28.
72. G. Milczarek, A. Kasuya, S. Mamykin, T. Arai, K. Shinoda, K. Tohji, *Int. J. Hydrogen Energy*, 28, (2003), 919.
73. T. Hellweg, *Curr. Opinion in Colloid & Interface Sci.*, 7, (2002), 50.
74. A. Manna, T. Imae, T. Yogo, K. Aoi, M. Okazaki, *J. Colloid Interface Sci.*, 256, (2002), 297.
75. M.P. Pileni, *Nature Materials*, 2, (2003), 145.
76. Y.R. Mahaddalkar, B.D. Bhawsar, *Physics Education*, April-June, (2002),

85.

77. *Physical Chemistry of Surfaces*, by A.W. Adamson, Wiley, New York, (1976), p: 490.
78. A. Lattes, I. Rico, A. De Savignac, A. Samii, *Tetrahedron*, 43, (1987), 1725.
79. L.M. Gan, C.H. Chew, *Bull. Singapur Natl. Inst. Chem.*, 23, (1995), 27.
80. J. Sjoblom, R. Lindberg, S.E. Friberg, *Adv. Colloid Interface Sci.*, 95, (1996), 125.
81. G.N. Kamau, N. Hu, J.F. Rusling, *Langmuir*, 8, (1992), 1042.
82. M.O. Iwunze, A. Sucheta, J.F. Rusling, *Anal. Chem.*, 62, (1990), 644.
83. G.N. Kamau, W.S. Willis, J.F. Rusling, *Anal. Chem.*, 57, (1985), 545.
84. J. Georges, J.W. Chen, *Colloid Polymer Sci.*, 264, (1986), 896.
85. J. Chen, O. Ikeda, K. Aoki, *J. Electroanal. Chem.*, 496, (2001), 88.
86. H. Hotta, N. Akagi, T. Sugihara, S. Ichikawa, T. Osakai, *Electrochem. Commun.*, 4, (2002), 472.
87. C. Minero, E. Pramauro, *Langmuir*, 4, (1988), 101.
88. G. Gounili, C.L. Miaw, J.M. Bobbitt, J.F. Rusling, *J. Colloid Interface Sci.*, 153, (1992), 446.
89. K. Asami, *Langmuir*, 21, (2005), 9032.